Geochemistry Geophysics Geosystems G3
AN ELECTRONIC JOURNAL OF THE EARTH SCIENCES
Published by AGU and the Geochemical Society

Article
Volume 5, Number 8
7 August 2004
Q08E17, doi:10.1029/2004GC000709
ISSN: 1525-2027

Glass compositions, plume-ridge interaction, and hydrous melting along the Galápagos Spreading Center, 90.5°W to 98°W

Buffy Cushman, John Sinton, and Garrett Ito
Department of Geology and Geophysics, University of Hawaii, 2525 Correa Road, Honolulu, Hawaii 96822, USA (bcushman@soest.hawaii.edu; sinton@hawaii.edu; gito@hawaii.edu)

Jacqueline Eaby Dixon
Rosenstiel School of Marine and Atmospheric Science, University of Miami, 4600 Rickenbacker Causeway, Miami, Florida 33149, USA (jdixon@rsmas.miami.edu)

[1] The Galápagos Spreading Center (GSC) between 90.5°W and 98°W manifests its interaction with the nearby Galápagos plume by way of variations in lava geochemistry, crustal thickness, and morphology along the ridge axis. Natural glasses from stations with ~9 km average spacing were analyzed for major and minor elements, H_2O, and CO_2. Samples can be classified as enriched mid-ocean ridge basalts (E-MORB), transitional MORB (T-MORB), or normal MORB (N-MORB) on the basis of K/Ti ratios. E-MORB dominate the GSC east of 92.6°W. T-MORB are mainly found between 92.6°W and 95.5°W. West of the propagating rift tip at 95.5°W, N-MORB dominate. High K/Ti E-MORB also have higher H_2O, Al_2O_3, and Na_2O and lower FeO*, SiO_2, and CaO/Al_2O_3 relative to N-MORB at similar values of MgO, characteristics consistent with lower mean extents of partial melting relative to N-MORB. We examine the melting process along this section of the GSC with a set of equations that simulate a deep zone of hydrous melting related to the depression of the mantle solidus by H_2O. This model constrains the range of mantle source compositions, the depth of the additional hydrous melting zone, the melt productivity in the hydrous region, and the ratio of mantle flow rate through the hydrous zone relative to the anhydrous zone (U_w/U_0) that can explain the measured crustal thickness as well as the fractionation-corrected concentrations of K, Na_2O, H_2O, and Ti along the GSC. Far from the hot spot, the measured crustal thickness and N-MORB compositions are explained by passive mantle upwelling ($U_w/U_0 = 1$), mean melt fraction ($\overline{F}$) ~ 0.06, and a source with ~35 ppm K, 130 ppm H_2O, 2300 ppm Na_2O, and 1050 ppm Ti. The transitional zone has a source enriched in K and could have a slight excess plume-driven flow through the hydrous melting zone ($U_w/U_0 \leq 1.5$). The crustal thickness and glass compositions in the "enriched" region of the GSC nearest the hot spot are best explained by only a slight increase in the temperature of the mantle (<~20°C), coupled with a mantle source moderately enriched (relative to N-MORB source) and plume-driven flow through the hydrous zone of $U_w/U_0 = 1.5–3.5$.

Components: 17,904 words, 13 figures, 5 tables.

Keywords: Galápagos plume; hot spot; mantle geochemistry; mid-ocean ridges; plume-ridge interaction.

Index Terms: 1025 Geochemistry: Composition of the mantle; 3035 Marine Geology and Geophysics: Midocean ridge processes; 8121 Tectonophysics: Dynamics, convection currents and mantle plumes.

Received 3 February 2004; **Revised** 31 May 2004; **Accepted** 28 June 2004; **Published** 7 August 2004.

Cushman, B., J. Sinton, G. Ito, and J. Eaby Dixon (2004), Glass compositions, plume-ridge interaction, and hydrous melting along the Galápagos Spreading Center, 90.5°W to 98°W, *Geochem. Geophys. Geosyst.*, *5*, Q08E17, doi:10.1029/2004GC000709.

Copyright 2004 by the American Geophysical Union

Theme: Plume-Ridge Interaction **Guest Editor:** David Graham

1. Introduction

[2] The global mid-ocean ridge system is affected by near- and on-axis hot spots, commonly thought to be caused by mantle plumes. Mantle plumes can impose large physical and chemical anomalies on otherwise normal ridges. These anomalies provide insight into processes that often cannot be studied as well from a "normal" mid-ocean ridge such as intermediate-wavelength variations in mantle flow and melting, mantle source composition and mixing, and the effects of variable magma supply on axial morphology, basalt chemistry, and crustal accretion. The Galápagos Spreading Center (GSC), with its intermediate spreading rate and off-axis plume, provides an excellent setting for studying these processes as they relate to plume-ridge interaction.

[3] The nearly east-west trending GSC separates the Cocos and Nazca plates in the eastern equatorial Pacific at a full opening rate of ~45–57 mm/yr in our study region [*DeMets et al.*, 1994] (Figure 1). At 91°W the GSC lies ~200 km north of the Galápagos Archipelago, the western end of which marks the probable center of the Galápagos mantle plume [*Geist*, 1992; *White et al.*, 1993]. Effects of the nearby hot spot are manifest in the regional bathymetric swell that extends ~1300 km along the ridge and peaks near 91°W, where the axial depth is more than 1 km shallower than portions of the ridge far from the hot spot, and in a regional mantle-Bouguer gravity anomaly that reaches its minimum (−70 mGal) near 91°W [*Canales et al.*, 2002]. The hot spot effect can also be seen in variations in axial morphology along the ridge [*Canales et al.*, 1997; *Detrick et al.*, 2002; *Sinton et al.*, 2003]. Within ~350 km of the Galápagos hot spot the GSC has an axial high morphology; with increased distance from the hot spot it changes to a transitional morphology, ultimately becoming a Mid-Atlantic-Ridge-like rift valley farthest from the hot spot (Figure 2).

[4] Several authors have examined the large-scale geochemical variations along the GSC, from 83°W to 101°W [*Christie and Sinton*, 1981; *Schilling et al.*, 1982, 2003; *Fisk et al.*, 1982; *Verma and Schilling*, 1982; *Sinton et al.*, 1983; *Verma et al.*, 1983; *Langmuir et al.*, 1992]. *Schilling et al.* [1982, 2003], *Verma and Schilling* [1982], and *Verma et al.* [1983] showed that rocks with high $^{87}Sr/^{86}Sr$ and incompatible element concentrations and low $^{143}Nd/^{144}Nd$ are confined to the region of the ridge closest to the hot spot. Normal mid-ocean ridge basalts (MORB) (i.e., those similar to MORB found in portions of the ocean-ridge system not associated with nearby hot spots) are found west and east of the 95.5°W and 85°W propagating rifts, respectively. These authors argued for a variably enriched mantle source nearest the hot spot, between 95.5°W and 85°W. *Langmuir et al.* [1992] showed that GSC lava compositions between 87°W and 95°W do not show the same relationship between chemical composition and axial depth as normal mid-ocean ridges.

[5] A major objective of the Galápagos Plume Ridge Interaction Multidisciplinary Experiment (G-PRIME) [*Detrick et al.*, 2002] is to better understand the processes of magma genesis along this hot spot-influenced ridge. Geophysical constraints on the rate of magma production are provided by measurements of crustal thickness from wide-angle seismic refraction experiments along three different portions of the GSC, as well as multichannel seismic reflection data gathered along and parallel to the ridge axis in the region 91.25°–95°W [*Canales et al.*, 2002]. Our geochemical sampling program obtained dredge and wax core samples at 91 stations between 90.5°–98°W; one station is within the transform zone near 90.5°W, all other sampling stations are along the ridge axis, with an average spacing between stations of ~9 km (Table 1, Figure 2). Sampling locations were chosen on the basis of multibeam bathymetric data collected during the cruise. In this paper we report major and minor element, H_2O and CO_2 data for G-PRIME (G′) glasses (Table 2). In addition, we reanalyzed selected glasses from the 95.5°W area [*Christie and Sinton*, 1981, 1986; *Yonover*, 1989; *Hey et al.*, 1992] in order to ensure uniform data quality and to augment the G′ data set. We incorporate these data, along with our seismic constraints on crustal thickness, into a simple, inverse model to examine the source compositions and conditions of melting along this hot spot-influenced section of the GSC.

2. Sample Treatment and Analyses

[6] Glass compositions were measured using the University of Hawaii Cameca SX-50, five-

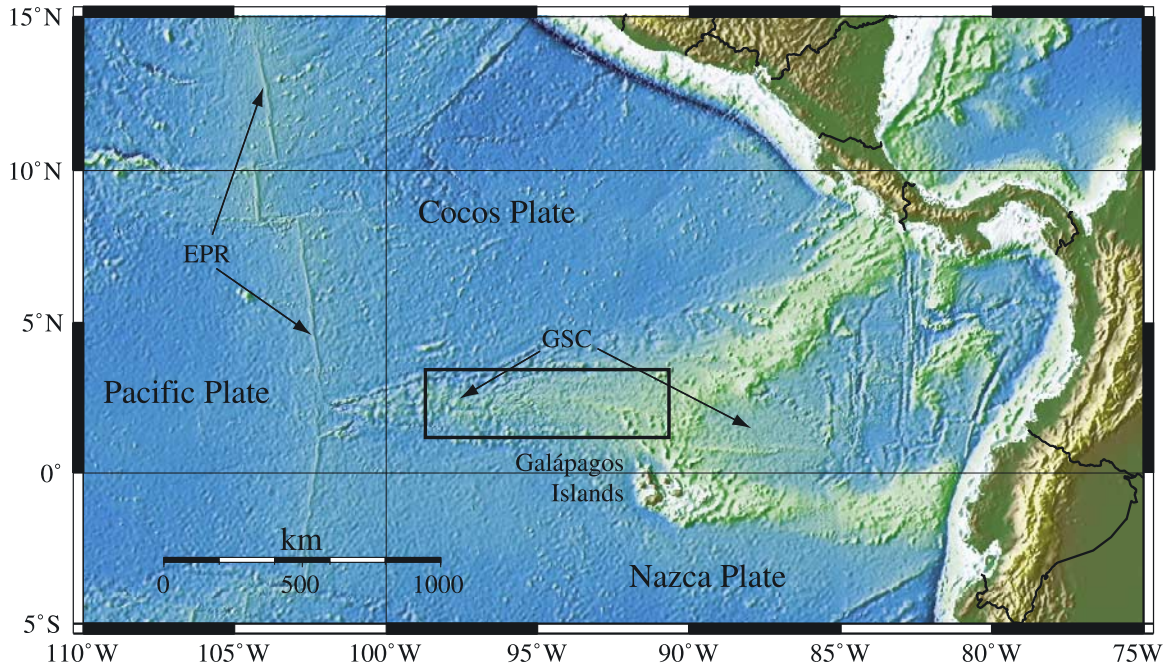

Figure 1. Location of Galápagos Spreading Center (GSC) relative to Central and South America, the East Pacific Rise (EPR), and the Galápagos Archipelago. The east-west trending GSC separates the Cocos and Nazca plates. The black box outlines the area of Figure 2.

spectrometer electron microprobe. Major and minor element analyses were obtained on glass chips from ~200 individual samples. Alvin samples and Atlantis dredge samples [*Hey et al.*, 1992] were reanalyzed using the same procedures. Reported analyses are averages of ten spots collected from three to six glass chips per sample, using an accelerating voltage of 15 kV, 10 nA beam current, and 10 μm beam diameter. Peak counting times were 110 seconds for P; 60 seconds for K; 50 seconds for Mn; 40 seconds for Fe; 30 seconds for Mg, Al, Si, Ca, and Ti; and 20 seconds for Na. Background counting times were 90 seconds for P; 30 seconds for K; 20 seconds for Mn; 10 seconds for Na, Ca, and Fe; and 5 seconds for Mg, Al, Si, and Ti. Samples were calibrated using Makaopuhi

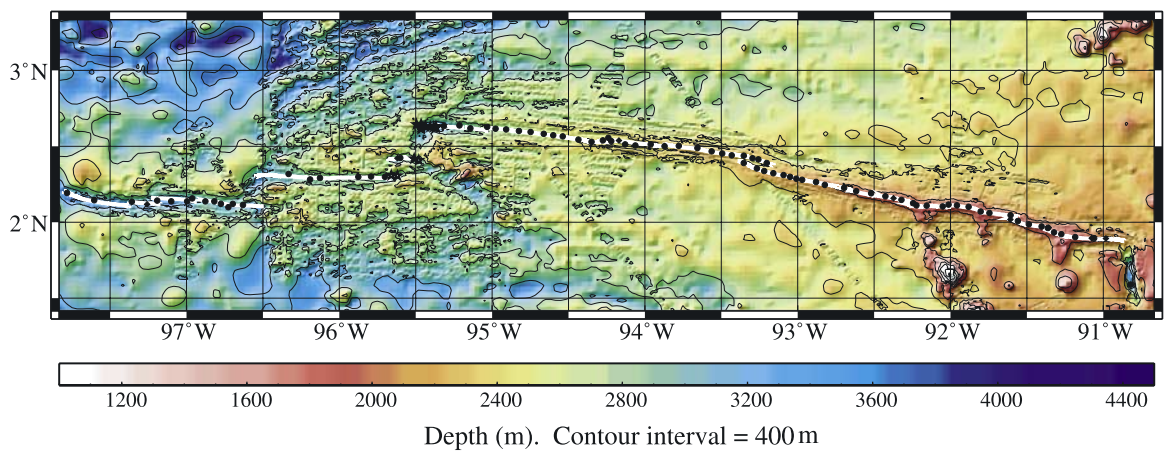

Figure 2. Bathymetric map of the study area based on multibeam data from *Sinton et al.* [2003] merged with satellite-derived seafloor topography data [*Smith and Sandwell*, 1997]. G′ sample stations (Table 1) are shown as circles (dredges) and diamonds (wax cores); Alvin samples from *Hey et al.* [1992] are shown as stars. The ridge axis is shown with a thin white line. Note transition from axial valley morphology in the west to axial high morphology in the east.

Table 1. Location and Estimated Recovery of Sampling Stations[a]

Stn	Type	Latitude	Longitude	Depth, m	Site Description	Recovery
2	dredge	1°35.3′N	90°49.0′W	3210	volcano in transform zone	~120 kg of glassy, aphyric pillow talus
3	wax core	1°53.4′N	90°59.2′W	2025	ridge tip near transform intersection	3 g glass
4	dredge	1°53.5′N	91°03.4′W	1962	ridge axis	~50 g glass fragments - lineated sheet lava
5	wax core	1°53.6′N	91°04.6′W	1916	ridge axis	2–3 g glass
6	dredge	1°54.1′N	91°10.8′W	1778	ridge axial high	5 pillow fragments
7	dredge	1°55.2′N	91°16.4′W	1635	ridge axis	5 kg pillow fragments
8	wax core	1°57.4′N	91°21.4′W	1377	"flat" top of volcano	1 g glass + sand
9	dredge	1°56.0′N	91°19.3′W	1583	axial high	150–200 kg sheet lava
10	dredge	1°57.6′N	91°21.7′W	1621	flat-topped, big volcano	5–10 kg sheet lava
11	dredge	1°58.3′N	91°24.1′W	1651	small ridge on axis	5 pillow fragments + 50 g glass
12	dredge	1°59.1′N	91°29.0′W	1672	small volcano on axial high	100 g glass chips
13	dredge	2°00.3′N	91°33.5′W	1732	south limb of osc	5–10 kg aphyric sheet lava
14	wax core	2°01.1′N	91°36.5′W	1821	top edge of axial volcano	4 g glass
15	dredge	2°02.7′N	91°36.3′W	1835	north limb of osc	150 kg aphyric, vesicular lava
16	dredge	2°03.6′N	91°44.6′W	1872	axial trough	10 kg Mn-crusted pillow talus
17	dredge	2°04.2′N	91°48.0′W	1762	60 m-high axial volcano	120 kg sheet lava
18	dredge	2°06.1′N	91°52.7′W	1683	flank of small axial volcano	200 g plag-phyric glass chips
19	dredge	2°06.6′N	91°57.3′W	1640	large axial volcano	30 kg lobate lava
20	dredge	2°06.9′N	92°00.5′W	1708	north limb of osc	60 kg lava fragments
21	dredge	2°06.2′N	92°03.1′W	1721	small high on axis	5–10 gm glass chips
22	dredge	2°06.4′N	92°09.4′W	1778	end of axial ridge	50 g glass chips
23	dredge	2°06.5′N	92°13.3′W	1850	narrow ridge tip	4 kg pillows + glass chips
24	dredge	2°07.5′N	92°14.6′W	1851	tip of north limb of osc	1 rock + glass chips
25	dredge	2°08.7′N	92°19.3′W	1818	axial graben	60 kg of glassy lava + pillar
26	wax core	2°09.5′N	92°22.4′W	1806	top of axial hill	25 g glass
27	dredge	2°10.2′N	92°25.6′W	1832	axial ridge	5–10 g glass
28	dredge	2°11.2′N	92°31.2′W	1863	local high at segment end	2 pillow fragments + glass
29	dredge	2°12.1′N	92°37.1′W	1920	narrow axial ridge	120 kg aphyric lava
30	dredge	2°13.4′N	92°41.7′W	2008	40 m-high volcano	~50 g glass shards
31	dredge	2°14.6′N	92°49.3′W	2098	axial deep	10 kg rock + glass
32	dredge	2°16.1′N	92°52.9′W	2126	volcanic mound in axis	2 pillow fragments with glass
33	dredge	2°16.9′N	92°58.4′W	2176	axial graben	6 kg pillow fragments
34	dredge	2°17.4′N	93°00.6′W	2167	axial graben	2 kg fresh, glassy ol + pl basalt
35	dredge	2°18.0′N	93°02.9′W	2211	axial graben	10 kg ol + pl pillow basalt
36	dredge	2°26.6′N	93°25.9′W	2273	south flank of axial volcano	~200 g glassy chips
37	dredge	2°23.6′N	93°21.2′W	2165	small volcano in axis	500 g glass shards
38	dredge	2°21.4′N	93°16.1′W	2293	north side of axial deep	Several rock fragments + glass
39	dredge	2°20.5′N	93°13.1′W	2331	axial graben	<1 kg glass chips
40	dredge	2°19.5′N	93°09.5′W	2231	small volcano in graben	8 kg pl + ol sheet flow fragments
41	dredge	2°18.8′N	93°05.6′W	2165	north side axial deep	150 kg big pillow fragments
42	dredge	2°23.5′N	93°12.3′W	2139	east tip of north limb of osc	~200 g pillow fragment + glass
43	dredge	2°24.7′N	93°15.3′W	2243	bump on ridge axis	2 kg pl + ol sheet flow fragments
44	dredge	2°25.2′N	93°17.7′W	2314	axial deep	200 g glass chips
45	dredge	2°26.6′N	93°21.1′W	2341	volcano in graben	20–25 kg pillows + glass
46	dredge	2°27.2′N	93°29.5′W	2319	small bump in axis	Glass fragments
47	dredge	2°27.8′N	93°33.7′W	2254	volcano in graben	One rock + glass
48	dredge	2°29.3′N	93°39.3′W	2305	small high in graben	~2 kg pillows + glass
49	dredge	2°30.0′N	93°52.1′W	2324	small ridge on axial high	5 kg rock + sediment + shrimp
50	dredge	2°30.0′N	93°46.5′W	2302	north flank of axial volcano	70 kg altered pillows (ol + pl)
51	dredge	2°30.6′N	93°57.7′W	2425	small rise in axial trough	<1 kg glassy, pl-phyric rock
52	dredge	2°30.2′N	94°03.6′W	2495	axial pit	<100 g glass
53	dredge	2°30.5′N	94°07.6′W	2509	deep, maybe off axis	10–15 kg mud + pillow fragments
54	wax core	2°32.3′N	94°10.3′W	2403	top of ridge	2 g aphyric glass
55	dredge	2°32.0′N	94°13.1′W	2471	flank of axial volcano	~100 g glass + sheet fragments
56	dredge	2°33.2′N	94°14.3′W	2478	ridge on axial high	200 kg pl + ol pillows
57	dredge	2°32.2′N	94°16.4′W	2515	irregular axial bump	200 g aphyric glassy rinds
58	dredge	2°31.6′N	94°20.9′W	2457	1 km volcano; south side of axis	150 kg porphyritic pillow basalt
59	dredge	2°32.5′N	94°25.9′W	2526	volcano on south side of graben	10 kg plag-phyric glassy pillows

Table 1. (continued)

Stn	Type	Latitude	Longitude	Depth, m	Site Description	Recovery
60	dredge	2°34.3′N	94°35.9′W	2612	high in axial graben	25 kg pl-phyric glassy buds
61	dredge	2°33.8′N	94°32.2′W	2608	local high in axial graben	1–2 kg of pillow fragments + glass
62	dredge	2°34.9′N	94°39.6′W	2691	bump in center of graben	75 kg big, pl-phyric pillows
63	dredge	2°35.5′N	94°44.7′W	2655	volcano in axial graben	500 g pl-phyric glass pieces
64	dredge	2°36.0′N	94°49.1′W	2766	axial rise structure	200 kg pl + ol pillows
65	dredge	2°36.6′N	94°54.4′W	2696	axial volcano	1.5 kg rock + glass
66	dredge	2°36.9′N	94°58.6′W	2763	axial high in graben	150 kg pl-phyric pillows
67	dredge	2°37.6′N	95°01.9′W	2621	big axial volcano	120 kg large pillows
68	dredge	2°37.0′N	95°08.4′W	2780	rise in axis	80 kg aphyric pillows
69	dredge	2°38.1′N	95°12.6′W	3065	high in axial valley	20 kg aphyric sheet fragments
70	dredge	2°37.8′N	95°18.9′W	3157	narrow axial ridge	25 kg ol + pl pillows and sheets
71	dredge	2°25.3′N	95°36.1′W	2768	ridge in north graben	30 kg pillow fragments
72	wax core	2°25.3′N	95°37.2′W	2800	ridge in north graben	4 g glass
73	dredge	2°17.9′N	95°42.0′W	2883	mound in axial graben	1 kg plag-phyric lava
74	dredge	2°17.9′N	95°47.5′W	2785	small volcano in graben	30 g plag-phyric glass chips
75	dredge	2°17.7′N	95°52.5′W	2957	base of south wall of graben	250 g pl + ol-phyric glass chunks
76	dredge	2°17.4′N	96°07.4′W	2829	irregular volcano	300 g porphyritic glass chunks
77	dredge	2°16.8′N	96°11.4′W	2851	small volcano caldera	<1 kg pl-phyric rock + glass
78	dredge	2°18.9′N	96°19.8′W	2948	small volcano in valley	<50 g sediment + glassy scoria
79	dredge	2°05.9′N	96°43.4′W	3136	small volcano in graben	30 kg pl-phyric pillows
80	dredge	2°06.8′N	96°37.7′W	3071	small volcano in valley	10 kg pl-phyric pillows and sheets
81	dredge	2°07.1′N	96°41.7′W	3062	volcano	70 kg hydrothermally altered pl-phyric pillows
82	dredge	2°07.2′N	96°46.5′W	3025	volcano	100 kg pl-phyric pillows
83	dredge	2°08.1′N	96°49.0′W	2957	small axial volcano	30 kg sheet lava
84	dredge	2°08.2′N	96°52.5′W	3042	elongate axial volcano	10 kg pl-phyric pillows
85	dredge	2°09.2′N	96°57.6′W	3113	axial volcano in graben	100 g pl-phyric glass
86	dredge	2°08.1′N	96°59.7′W	3274	medium axial volcano	150 g pl-phyric glassy pillows
87	dredge	2°08.2′N	97°05.9′W	3272	volcano flank in axis	20 kg pl-phyric sheets and pillows
88	dredge	2°08.4′N	97°11.5′W	3229	circular volcano	45 kg pl-phyric pillows
89	dredge	2°08.0′N	97°21.4′W	3215	volcanic ridge	50 g glass
90	wax core	2°07.1′N	97°15.5′W	3327	side of ridge in graben	2 flecks of glass
91	dredge	2°08.5′N	97°36.2′W	3440	volcano on ridge	150 kg hydrothermally altered pillows and sheets
92	dredge	2°11.5′N	97°46.9′W	3360	irregular volcano	200 kg sheets and pillows

[a] Stn, dredge or wax core station number; osc, Overlapping Spreading Center; ol, olivine; pl, plagioclase.

glass standard A-99 (Mg, Si, Ti, Fe), Juan de Fuca glass standard VG-2 (Na, Al, Ca), and mineral standards apatite (P) and orthoclase (K). A PAP matrix correction was applied to all analyses.

[7] The number of individual samples analyzed per dredge varied between 1 and 12, depending on the size of the dredge haul. Dredges were dragged over ~200–500 meters of seafloor, so it is possible that rocks in a dredge haul include samples from more than one eruptive unit. Individual samples from each station with compositions that agreed within ~5–10% in the low-abundance oxides K_2O, P_2O_5, TiO_2, and Na_2O were designated as a single group. High-abundance element concentrations were compared for consistency of the groupings; in all cases some variance between groups is observed in all elements. Most dredges contain only one group; the maximum number of groups in a dredge is three (dredges 41, 55). Once groups were determined, all analyses for samples from that group were averaged (Table 2). Each group probably represents a single lava flow or group of closely related flows. An estimate of the precision of the microprobe data is reported as one standard deviation from the mean for groups containing 9 or more individual samples (Table 2).

[8] On the basis of major element composition and along-axis locations, one glass sample from each of 42 of the groups was analyzed for dissolved H_2O and CO_2 using infrared spectroscopy at the University of Miami following the procedures of *Dixon and Clague* [2001]. Precision of the analyses is about ±2% for total water, and ±7 to 10% for molecular water and carbonate. Because of the larger uncertainty in the compositional dependence of the molar absorptivity for water dissolved as molecular water and carbon dissolved as carbonate in silicate glasses, the accuracy of the molecular

Table 2. Glass Compositions[a]

Group[b]	*n*	Type[c]	SiO_2	TiO_2	Al_2O_3	FeO*	MnO	MgO	CaO	Na_2O	K_2O	P_2O_5	H_2O	CO_2	Total	Sample[d]
2D	9	N	49.5	0.81	15.8	9.71	0.18	9.24	12.7	1.72	0.03	0.05	0.075	173	99.9	2D-1
3C	1	E	49.7	1.89	13.7	12.8	0.22	6.40	11.1	2.64	0.21	0.17			98.8	
4D	5	T	49.1	1.50	15.5	10.2	0.19	7.99	12.2	2.51	0.12	0.13	0.248	144	99.7	4D-1
5C	1	E	49.7	1.85	14.1	11.6	0.22	6.79	11.6	2.66	0.21	0.16			98.9	
6D	5	T	50.1	1.41	14.4	11.1	0.19	7.54	12.2	2.33	0.11	0.11			99.5	
7D-a	1	E	49.8	1.87	14.3	11.7	0.21	6.79	11.3	2.71	0.23	0.18	0.400	137	99.5	7D-4
7D-b	2	T	49.2	1.80	14.8	10.8	0.19	7.22	12.0	2.75	0.18	0.15			99.1	
8C	1	E	50.0	2.75	13.3	13.9	0.24	5.00	9.27	3.04	0.48	0.31			98.2	
9D-a	6	T	49.7	1.88	14.3	11.5	0.19	6.93	11.6	2.72	0.17	0.15	0.341	189	99.5	9D-1.1
9D-b	6	T	49.2	1.64	15.4	10.4	0.19	7.76	11.9	2.61	0.15	0.13			99.4	
10D	4	E	50.3	2.83	13.3	14.0	0.24	4.88	9.32	2.98	0.49	0.32	0.722	57	99.3	10D-1
11D-a	3	E	53.2	2.57	13.2	13.3	0.22	3.33	7.43	3.28	0.82	0.51	1.077		98.9	11D-1
11D-b	1	E	51.7	2.95	13.1	14.0	0.27	3.98	8.14	3.25	0.71	0.50			98.7	
12D	6	E	50.4	2.98	12.9	14.5	0.24	4.60	8.88	3.07	0.51	0.39	0.793		99.2	12D-5
13D	6	E	50.0	2.90	13.3	13.6	0.23	4.90	9.34	2.93	0.57	0.39			98.2	
14C	1	E	50.4	3.21	12.5	15.2	0.27	4.20	8.51	2.85	0.52	0.41			98.1	
15D	5	T	49.6	1.49	14.8	10.4	0.19	8.02	11.9	2.20	0.17	0.15	0.304	176	99.1	15D-1
16D	3	E	48.2	2.16	15.7	10.6	0.19	6.77	10.8	3.10	0.31	0.25	0.574	141	98.7	16D-2
17D-a	6	E	47.6	2.00	16.7	9.43	0.16	7.20	11.0	3.32	0.38	0.27	0.612	96	98.7	17D-4
17D-b	2	E	47.6	1.93	16.9	9.28	0.16	7.63	11.0	3.25	0.36	0.25			98.3	
18D	6	E	49.0	1.57	15.0	10.1	0.18	7.54	12.0	2.56	0.23	0.17			98.4	
19D	9	E	50.4	2.73	13.4	13.6	0.24	4.79	9.08	3.24	0.47	0.34	0.819		99.1	19D-1
20D-a	2	E	48.1	1.63	16.6	9.60	0.16	8.14	11.9	2.59	0.27	0.18	0.441	175	99.6	20D-1
20D-b	3	E	48.6	1.73	16.2	9.80	0.16	7.72	11.7	2.75	0.29	0.20			99.1	
21D	1	E	49.3	2.06	14.6	11.2	0.21	6.51	11.2	3.01	0.32	0.21			98.5	
22D	1	E	49.3	2.24	14.7	10.8	0.20	6.45	11.7	3.09	0.41	0.27			99.2	
23D	1	E	49.9	1.86	14.2	11.5	0.20	6.52	11.3	2.74	0.26	0.18			98.6	
24D	2	E	49.8	1.84	14.6	10.7	0.21	6.98	11.5	2.55	0.26	0.20			98.6	
25D-a	3	E	49.6	1.63	15.1	10.2	0.18	7.17	11.9	2.54	0.27	0.18	0.383	187	99.2	25D-1
25D-b	3	E	49.4	1.61	15.0	10.2	0.18	7.55	11.8	2.52	0.26	0.16			98.8	
26C	1	E	50.0	1.67	14.8	10.2	0.18	6.83	11.4	2.59	0.48	0.20			98.3	
27D	1	E	50.2	2.06	13.6	12.6	0.25	6.14	10.7	2.50	0.22	0.20			98.4	
28D	4	E	50.2	1.57	14.3	10.9	0.20	7.08	11.9	2.41	0.22	0.14	0.328	97	99.2	28D-1
29D	5	T	50.4	1.67	13.9	11.8	0.21	6.84	11.2	2.42	0.16	0.14	0.301	170	99.1	29D-1
30D	1	E	50.3	2.13	13.2	13.4	0.24	5.81	10.3	2.59	0.23	0.21			98.5	
31D	4	T	50.1	1.82	13.7	12.5	0.21	6.42	10.8	2.63	0.18	0.15			98.5	
32D	2	T	50.3	1.66	13.7	12.4	0.22	6.79	11.1	2.21	0.14	0.14			98.5	
33D	6	T	50.4	1.61	13.7	12.6	0.22	6.72	10.9	2.32	0.14	0.13	0.269	168	99.0	33D-1
34D-a	2	T	50.2	1.49	14.2	11.5	0.21	7.22	11.7	2.24	0.13	0.12			99.1	
34D-b	3	T	50.5	1.53	14.1	11.7	0.19	7.08	11.7	2.34	0.13	0.14			99.5	
35D-a	2	T	50.6	1.74	13.8	12.5	0.22	6.50	11.2	2.54	0.14	0.15			99.4	
35D-b	1	T	50.8	1.81	13.5	12.8	0.24	6.40	11.2	2.59	0.15	0.15			99.6	
36D	1	T	50.8	1.57	14.1	11.8	0.21	7.06	11.3	2.34	0.15	0.16			99.5	
37D	4	T	50.9	1.33	14.3	11.2	0.20	7.32	12.1	2.25	0.11	0.11			99.8	
38D	3	T	50.9	1.72	13.8	12.4	0.22	6.68	11.3	2.33	0.14	0.17	0.296	182	99.9	38D-2
39D-a	2	T	51.0	1.72	13.8	12.5	0.21	6.57	11.2	2.40	0.15	0.16			99.7	
39D-b	1	T	50.9	1.44	14.4	11.0	0.19	7.37	12.2	2.29	0.16	0.13			100.1	
40D	5	T	50.3	0.99	15.3	9.49	0.17	8.67	13.3	1.96	0.07	0.08			100.3	
41D-a	1	T	50.7	1.33	14.5	11.2	0.21	7.56	12.0	2.26	0.11	0.12			100.0	
41D-b	3	T	50.7	1.24	14.6	11.0	0.20	7.69	12.2	2.23	0.11	0.11	0.198	201	100.3	41D-7
41D-c	3	T	50.8	1.38	14.2	11.5	0.20	7.27	11.9	2.26	0.12	0.13	0.219	233	100.0	41D-1
42D-a	2	N	50.8	0.77	14.9	9.28	0.18	8.90	13.6	1.67	0.05	0.06			100.2	
42D-b	2	T	50.7	0.86	14.9	9.57	0.18	8.78	13.3	1.73	0.06	0.07			100.1	
43D	2	N	50.4	0.89	14.9	9.27	0.18	8.70	13.5	1.90	0.04	0.05	0.101	202	99.9	43D-1
44D	1	T	49.5	1.10	15.5	9.91	0.18	8.58	12.5	2.10	0.08	0.07			99.5	
45D	3	T	50.2	1.26	15.0	10.4	0.18	8.03	12.0	2.27	0.09	0.08	0.200	169	99.6	45D-2
46D	2	T	50.8	1.24	14.5	10.4	0.19	7.84	12.4	2.18	0.11	0.08			99.7	
47D	2	T	50.6	1.66	13.9	12.1	0.22	6.71	11.2	2.52	0.16	0.13			99.3	
48D	3	N	50.3	1.18	14.8	10.3	0.20	8.05	12.5	2.24	0.07	0.07	0.299	146	100.0	48D-4
49D	2	T	50.7	1.73	13.6	12.7	0.22	6.58	10.8	2.57	0.15	0.12	0.308	193	99.6	49D-1
50D	5	T	50.6	1.32	14.5	10.5	0.20	7.80	12.2	2.24	0.14	0.10	0.216	142	99.9	50D-1
51D	3	T	50.7	1.30	14.4	10.7	0.20	7.70	12.5	2.34	0.09	0.07			99.9	

Table 2. (continued)

Group[b]	*n*	Type[c]	SiO_2	TiO_2	Al_2O_3	FeO*	MnO	MgO	CaO	Na_2O	K_2O	P_2O_5	H_2O	CO_2	Total	Sample[d]
52D	1	T	50.7	1.63	14.0	12.0	0.21	6.94	11.3	2.58	0.14	0.12			99.5	
53D	4	T	50.9	1.94	13.3	13.4	0.23	6.10	10.6	2.55	0.15	0.14			99.2	
54C	1	T	50.2	1.21	15.4	9.70	0.16	8.40	12.4	2.09	0.11	0.07			99.7	
55D-a	2	T	50.7	1.56	14.1	11.6	0.21	7.19	11.5	2.30	0.15	0.13			99.4	
55D-b	2	T	50.7	1.75	13.8	12.3	0.22	6.76	11.0	2.43	0.18	0.15			99.2	
55D-c	1	T	50.7	1.82	13.7	12.5	0.21	6.65	10.9	2.38	0.19	0.15			99.1	
56D	5	T	50.5	1.42	14.4	11.3	0.20	7.42	11.8	2.31	0.11	0.10	0.227	155	99.7	56D-2
57D	1	T	50.8	1.78	13.7	12.3	0.24	6.54	11.0	2.45	0.19	0.15			99.1	
58D	4	T	50.5	1.56	14.0	12.1	0.21	7.03	11.4	2.40	0.12	0.10	0.252	183	99.6	58D-2
59D	3	T	51.2	1.27	14.4	10.5	0.20	7.55	12.0	2.22	0.10	0.10			99.6	
60D	4	T	50.5	1.34	14.6	10.9	0.20	7.74	12.1	2.15	0.09	0.12			99.7	
61D	5	T	51.0	1.29	14.5	10.5	0.20	7.64	12.3	2.21	0.10	0.11			99.8	
62D	5	T	49.2	1.28	15.4	10.8	0.18	7.97	11.7	2.40	0.09	0.11	0.215	190	99.4	62D-1
63D-a	1	N	50.4	1.31	14.4	10.6	0.19	7.79	12.2	2.15	0.06	0.10	0.172	216	99.5	63D-1
63D-b	1	T	49.3	1.28	15.4	10.9	0.20	7.99	11.7	2.40	0.09	0.12	0.211	216	99.6	63D-2
64D	5	T	50.7	1.55	14.3	11.0	0.20	7.13	11.7	2.44	0.13	0.16			99.3	
65D	1	T	51.0	1.32	14.3	10.9	0.18	7.52	12.1	2.05	0.10	0.11			99.7	
66D	7	N	50.6	1.23	15.1	10.2	0.18	8.31	12.2	2.08	0.08	0.10			100.1	
67D	3	T	50.1	1.41	15.1	10.6	0.18	8.01	11.8	2.25	0.11	0.13	0.265	184	100.0	67D-1
68D-a	2	T	50.4	1.68	14.3	11.6	0.21	7.54	11.2	2.25	0.14	0.17			99.6	
68D-b	3	T	50.4	1.68	14.2	11.6	0.21	7.79	11.1	2.23	0.14	0.16			99.4	
69D	2	T	50.4	1.65	14.1	11.8	0.20	7.72	11.1	2.28	0.13	0.16	0.288	166	99.9	69D-1
70D	5	T	50.6	1.58	14.5	11.2	0.19	7.72	11.5	2.24	0.11	0.15	0.259	201	100.1	70D-1
71D-a	3	N	49.5	1.00	16.3	9.03	0.16	9.52	12.5	2.16	0.04	0.07	0.153	228	100.4	71D-1
71D-b	1	N	49.7	1.02	16.5	9.04	0.16	9.12	12.7	2.17	0.04	0.08			100.4	
72C	1	N	50.6	1.20	15.5	9.43	0.17	8.58	12.4	2.15	0.07	0.09			100.1	
73D	1	T	48.8	0.92	17.1	9.31	0.18	9.29	12.3	2.27	0.07	0.06	0.144	170	100.5	73D-1
74D	1	N	50.2	1.10	15.5	9.18	0.19	8.56	12.7	2.23	0.05	0.08			99.8	
75D	2	N	51.1	1.42	14.4	11.1	0.21	7.26	11.7	2.56	0.08	0.11	0.221		100.1	75D-1
76D	2	N	50.9	1.10	15.1	9.46	0.18	8.34	12.7	2.06	0.06	0.09			100.0	
77D-a	1	N	50.6	1.22	15.1	9.81	0.18	8.20	12.6	2.23	0.05	0.10			100.1	
77D-b	2	N	50.8	1.27	14.9	10.0	0.19	7.97	12.4	2.28	0.05	0.10	0.157	226	100.2	77D-1
78D	2	E	48.5	3.09	14.1	11.8	0.22	6.14	11.3	3.00	0.55	0.36	0.181	151	99.2	78D-1
79D	4	N	49.0	1.01	16.7	9.73	0.18	8.87	12.0	2.48	0.04	0.07	0.160	296	100.4	79D-1
80D	5	N	49.9	1.13	15.8	9.15	0.17	8.70	12.6	2.51	0.03	0.08	0.109		100.1	80D-2
81D	5	N	48.8	0.90	17.0	8.24	0.15	9.55	12.7	2.33	0.03	0.05			99.8	
82D	9	N	48.1	1.01	17.5	8.88	0.15	9.28	12.1	2.48	0.02	0.06			99.6	
83D	5	N	49.9	1.23	15.6	9.51	0.17	8.60	12.0	2.23	0.05	0.09			99.3	
84D	4	N	50.3	1.30	14.6	9.82	0.18	7.95	12.3	2.19	0.06	0.11	0.154	219	98.9	84D-4
85D	1	N	50.5	1.34	14.5	9.77	0.19	7.88	12.3	2.35	0.05	0.10			99.0	
86D-a	2	N	50.1	1.25	14.7	9.63	0.18	8.17	12.3	2.09	0.06	0.10			98.6	
86D-b	2	N	49.9	1.35	14.9	9.85	0.17	8.27	12.2	2.10	0.06	0.11			98.9	
87D	5	N	50.4	1.18	15.1	9.30	0.17	8.35	12.7	2.24	0.05	0.09			99.5	
88D	5	N	50.5	1.16	15.1	9.20	0.16	8.56	12.6	2.08	0.05	0.08	0.130	202	99.7	88D-1
89D	3	N	50.7	1.31	14.8	9.66	0.18	8.13	12.4	2.13	0.06	0.10			99.4	
90C-a	1	N	50.9	1.68	14.0	11.8	0.21	6.82	11.4	2.21	0.08	0.14			99.3	
90C-b	2	N	50.6	1.59	14.2	10.7	0.20	7.46	11.8	2.38	0.07	0.12			99.1	
91D	10	N	50.0	1.09	15.5	9.11	0.17	8.95	12.5	2.06	0.04	0.08			99.5	
92D	6	N	50.0	1.39	15.0	9.76	0.17	8.46	11.9	2.25	0.07	0.12	0.186	237	99.3	92D-1
1538	4	T	50.7	1.76	14.0	11.9	0.20	6.99	11.2	2.34	0.13	0.16			99.5	
1539-a	2	T	50.6	1.70	14.2	11.9	0.21	7.21	11.3	2.37	0.12	0.14			99.8	
1539-b	1	T	51.0	1.84	13.6	12.5	0.22	6.57	11.3	2.35	0.14	0.17			99.8	
1540-a	3	T	51.0	1.92	13.4	13.1	0.22	6.29	11.0	2.40	0.15	0.16			99.5	
1540-b	3	T	51.0	1.59	14.2	11.8	0.21	7.25	11.4	2.32	0.12	0.13			100.0	
1541	2	T	51.2	1.57	14.1	11.7	0.21	7.13	11.4	2.34	0.12	0.14			99.9	
1544	2	N	51.1	1.69	13.9	11.8	0.20	7.05	11.7	2.29	0.11	0.15			100.0	
1545-a	3	T	50.6	1.78	14.1	11.9	0.19	7.18	11.2	2.30	0.13	0.16			99.5	
1545-b	3	N	50.3	1.05	15.4	9.62	0.17	8.79	12.7	1.88	0.05	0.08			100.0	
1549-a	3	T	50.8	1.67	14.1	11.9	0.21	7.45	11.2	2.31	0.13	0.15			100.0	
1549-b	3	N	50.6	0.99	15.5	9.62	0.17	8.86	13.0	1.87	0.05	0.07			100.7	
1551-a	2	N	49.9	1.11	16.2	9.35	0.16	8.60	12.6	2.46	0.05	0.09			100.4	
1551-b	2	T	50.4	1.14	15.6	9.73	0.16	9.00	11.8	2.31	0.08	0.09			100.3	

Table 2. (continued)

Group[b]	*n*	Type[c]	SiO_2	TiO_2	Al_2O_3	FeO*	MnO	MgO	CaO	Na_2O	K_2O	P_2O_5	H_2O	CO_2	Total	Sample[d]
1554-a	3	N	49.9	1.12	16.3	9.46	0.16	8.77	12.4	2.36	0.05	0.08			100.6	
1554-b	1	N	50.4	1.29	15.8	10.0	0.19	8.39	12.0	2.38	0.06	0.09			100.6	
1554-c	3	N	50.3	0.95	16.1	8.60	0.17	9.13	13.1	2.16	0.05	0.06			100.6	
1554-d	3	N	49.6	1.04	16.5	9.15	0.16	9.67	12.2	2.25	0.04	0.07			100.6	
1555	10	N	51.1	1.14	15.1	9.59	0.17	8.48	12.6	2.11	0.06	0.08			100.5	
1557-a	1	T	50.8	1.88	13.3	13.3	0.23	6.31	10.9	2.39	0.15	0.16			99.4	
1557-b	1	T	50.8	1.66	13.8	12.4	0.24	6.85	11.3	2.34	0.13	0.15			99.7	
1557-c	6	T	51.0	1.55	14.2	11.8	0.20	7.23	11.4	2.33	0.12	0.14			99.9	
A6	7	T	50.6	1.71	14.0	12.0	0.21	7.47	11.0	2.32	0.13	0.15			99.5	
A13	4	N	51.1	1.25	14.6	10.1	0.19	7.97	12.4	2.13	0.08	0.10			99.9	
Precision[e]			0.1	0.015	0.05	0.06	0.01	0.07	0.05	0.03	0.01	0.01				

[a] All values in wt%, except CO_2 (ppm). Major and minor elements by University of Hawai'i electron microprobe; H_2O and CO_2 by University of Miami FTIR. FeO* is total Fe as FeO. Compositions for major and minor elements are averages for all individual samples within a group; *n* indicates the number of individual samples averaged in each group.

[b] Sample group names are the station number followed by the sampling method: D for dredge or C for wax core. Alvin and Atlantis samples [*Hey et al.*, 1992] are named according to the four-digit dive number or dredge number (preceded by A). Multiple groups per station are designated as a, b, or c.

[c] MORB types (see text).

[d] Individual sample number analyzed by FTIR.

[e] Precision for the major and minor element analyses based on standard deviations of groups containing nine or more individual samples.

water and carbonate analyses is estimated to be about ±20%.

3. Observations

3.1. Classification of MORB Types

[9] To assess potential differences in parental magma compositions, we use K/Ti ratios to divide our samples (Figure 3) [*Schilling et al.*, 1983; *Hekinian et al.*, 1989; *Sinton et al.*, 1991; *Langmuir et al.*, 1992], because K/Ti is relatively unaffected by fractionation processes at MgO values greater than that at which FeTi oxide appears as a fractionating phase (~4.5 wt% MgO in G′ samples; see Figures 4c and 4e). G′ samples can be divided into three general types: enriched (E-) MORB, with K/Ti ratios >0.15 and K_2O contents >0.20% (all percentages are given in weight percent); transitional (T-) MORB, with K/Ti ratios mainly between 0.09 and 0.15; and normal (N-) MORB, with K/Ti ratios <0.09 (Figure 3). K/Ti

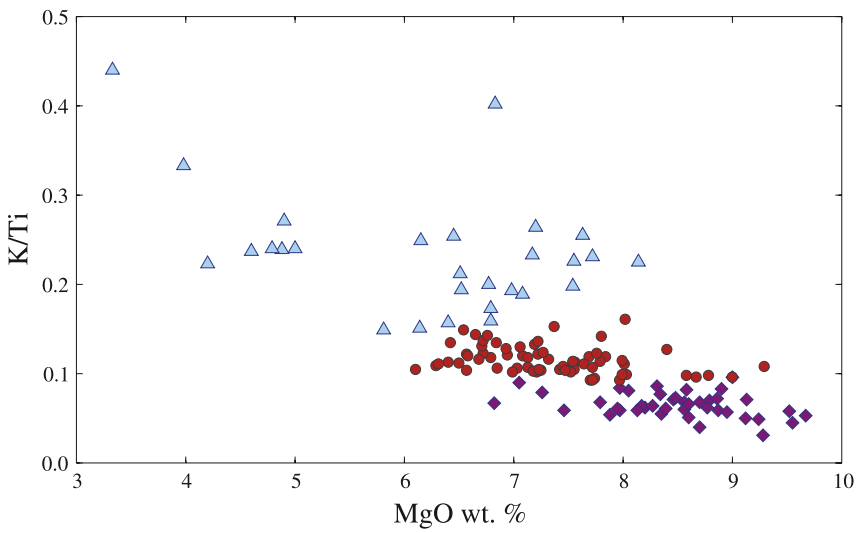

Figure 3. Classification based on K/Ti versus MgO: Samples with K/Ti < 0.09 are designated as N-MORB (purple diamonds); T-MORB (red circles) have K/Ti between 0.09 and ~0.15; E-MORB (light blue triangles) have K/Ti > 0.15 and K_2O > 0.20. See text for discussion.

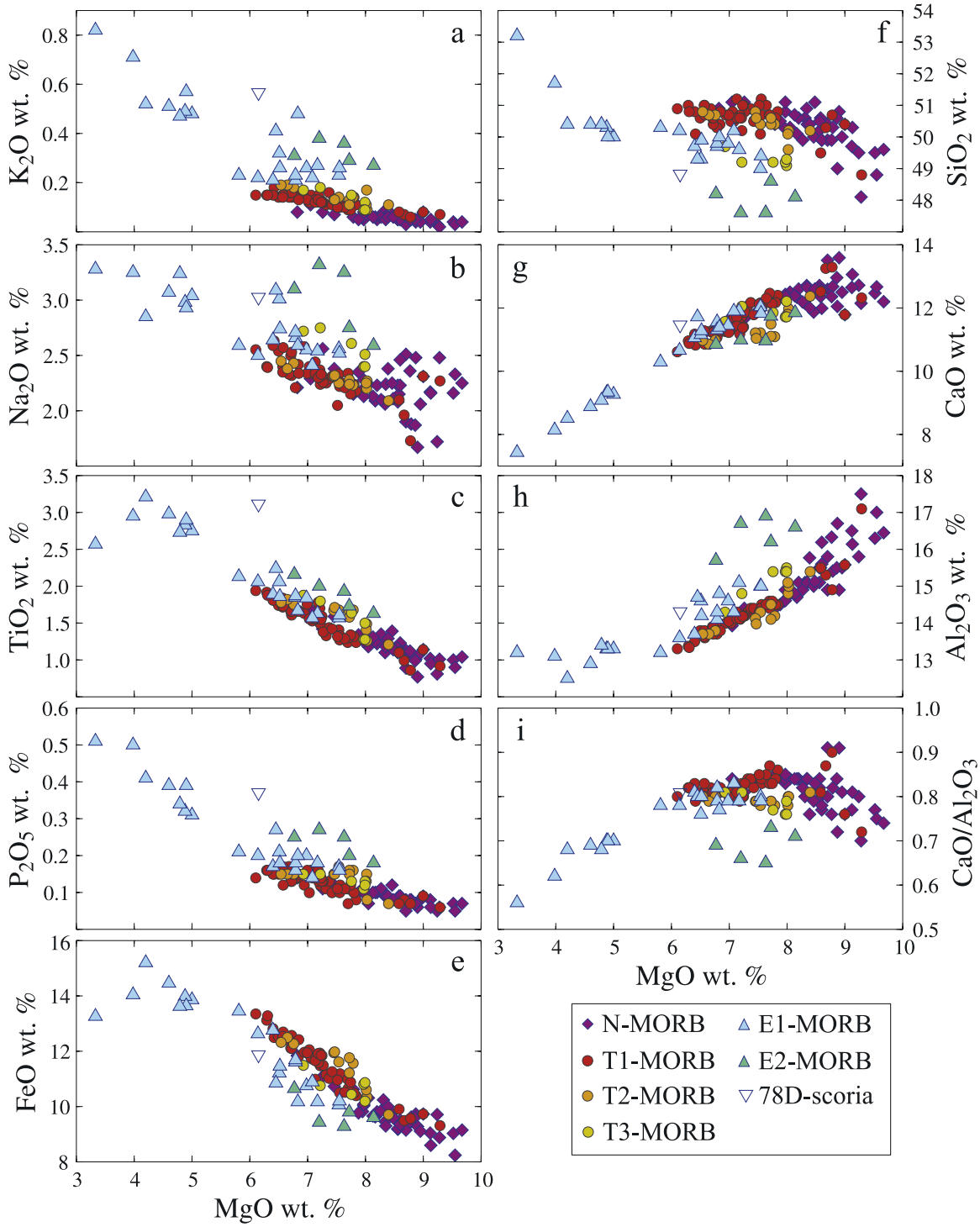

Figure 4. Major element oxides plotted versus MgO. Variation among MORB types (see text for discussion) shown in the legend.

ratios alone effectively discriminate the three sample groups. Most MORB with K/Ti > 0.15 have K_2O abundances >0.20%, and are therefore "enriched" in the more incompatible element, K. However, two sample groups (15D and 39D-b) have K/Ti > 0.15 but K_2O < 0.20%. On most plots, including those involving trace element data not reported here, these samples follow trends associated with T-MORB. Thus we restrict the definition of GSC E-MORB in this paper to

sample groups with K/Ti > 0.15 and K_2O > 0.20%.

[10] Although the threefold division accounts for most of the compositional diversity, it is apparent that significant variability at constant MgO, especially in SiO_2 and Al_2O_3, is present within the E- and T-MORB types (Figures 4e–4i). We have therefore subdivided these types as follows: Relative to most E-MORB (hereafter E1-MORB), E2-MORB have anomalously low SiO_2 and high CaO/Al_2O_3, the latter because of both lower CaO and higher Al_2O_3 than E1-MORB. T2-MORB have slightly higher incompatible element values, particularly K_2O, relative to "regular" T1-MORB. T3-MORB have low CaO/Al_2O_3 ratios, and low SiO_2, as well as higher Na_2O and K_2O than T1-MORB.

3.2. Compositional Variations

[11] Variations in glass compositions with MgO (Figure 4) indicate large variations in fractional crystallization along the GSC. The least differentiated of all G′ samples are N-MORB, which have MgO values that range from 6.9% to almost 10%. Slight changes in the slopes of MgO versus CaO, SiO_2, and CaO/Al_2O_3 for N-MORB show that plagioclase joins olivine in the fractionating assemblage between ~8.0 and 8.5% MgO. N-MORB are characterized by low concentrations of elements that are incompatible during mantle melting: ≤0.08% K_2O, 1.67–2.56% Na_2O, 0.77–1.68% TiO_2, 0.05–0.12% P_2O_5. N-MORB have the lowest H_2O concentrations of all G′ samples, with no values greater than 0.22% (Figure 5a). These "normal" MORB values are typical of, or even slightly lower than, H_2O values found along other "normal" portions of the global mid-ocean ridge system [*Michael*, 1988, 1995; *Dixon et al.*, 1988; *Danyushevsky et al.*, 2000].

[12] As a group, T-MORB are slightly more differentiated than N-MORB, with MgO contents ranging from 6.1 to 9.3%, and with the bulk of the samples having MgO < 8.0% (Figure 4). T-MORB are most distinct from N-MORB in K_2O, giving rise to their higher K/Ti ratios. T-MORB have average values of incompatible oxides Na_2O, P_2O_5, TiO_2, and FeO* (total Fe reported as FeO) higher than in N-MORB because the N-MORB tend to be less fractionated, but the differentiation trends are collinear. Differentiation trends for the T-MORB also are collinear with those for N-MORB for CaO, Al_2O_3, and SiO_2. As with the N-MORB, changes in the slope of CaO and SiO_2 trends for the T-MORB indicate plagioclase fractionation beginning between ~8.0 and 8.5% MgO.

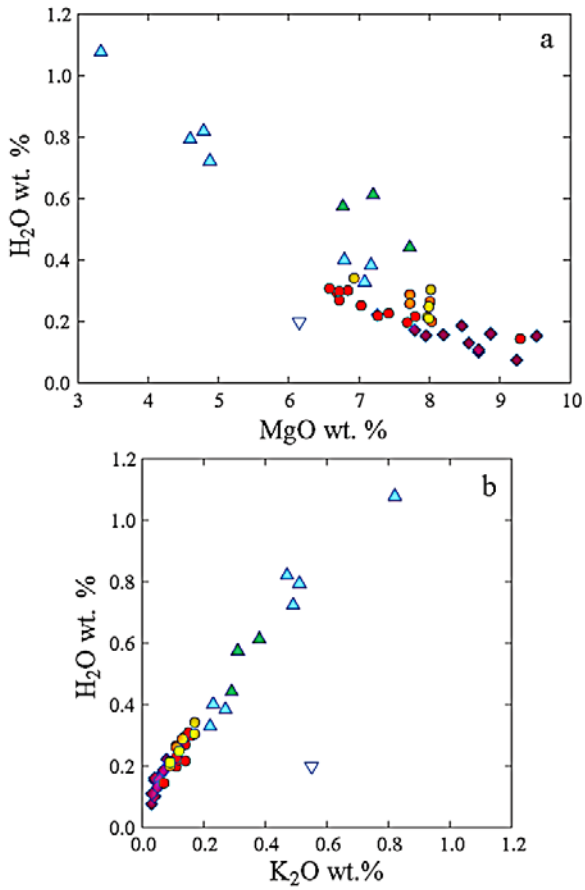

Figure 5. H_2O versus (a) MgO and (b) K_2O. Symbols as in Figure 4. The incompatible nature of H_2O is evident from the positive correlation with K_2O; the slope indicates that the bulk distribution coefficient (D) for K_2O is less than D_{H2O}.

[13] T2-MORB differ from T1-MORB in CaO/Al_2O_3, mostly because of lower CaO. T2-MORB also are enriched slightly in TiO_2, K_2O, and H_2O relative to T1-MORB. T3- MORB have much lower CaO/Al_2O_3 than T1-MORB, as a result of both lower CaO and higher Al_2O_3 at a given value of MgO. T3-MORB have significantly lower SiO_2 than T1-MORB, and are slightly enriched relative to T1-MORB in Na_2O, K_2O, TiO_2, P_2O_5, and H_2O.

[14] E-MORB are more differentiated than N- and T-MORB, with MgO contents ranging to values as low as 3.3% (Figure 4). E-MORB are enriched relative to N- and T-MORB in K_2O, Na_2O, P_2O_5, and H_2O. TiO_2 values are slightly higher at a given MgO value in E-MORB than in T-MORB. Lower relative FeO* and SiO_2, and higher Al_2O_3 values

Table 3. Empirical Slopes Calculated for $MgO_{(8.0)}$ Adjustments[a]

	Linear Regressions				Power Law Regressions				
MORB Type	SiO_2	Al_2O_3	FeO*	CaO	TiO_2	Na_2O	K_2O	P_2O_5	H_2O
N	−0.31	0.79	−1.28	0.55	−1.59	−0.51	−1.41	−1.89	−2.70
T	−0.31	0.79	−1.28	0.55	−1.59	−0.51	−1.99	−1.89	−2.70
E	−0.27	0.68	−1.28	1.13	−1.28	−0.34	−1.61	−1.66	−1.57

[a] Linear regressions were applied to SiO_2, Al_2O_3, FeO*, and CaO; power law regressions ($y = a*x^m$, where the shown numbers are values of m) were applied to incompatible elements TiO_2, Na_2O, K_2O, P_2O_5, and H_2O. Samples with MgO < 3.5 wt% or > 8.5 wt% were excluded from the regressions, with the exception that regression of CaO, Na_2O, K_2O, P_2O_5, and H_2O in E-MORB includes samples with <3.5 wt.% MgO; E-MORB trends for these oxides are not affected by the appearance of new fractionating phases at this composition. No T2, T3, or E2 samples were used to calculate slopes of lines or curves, with the exception of H_2O, for which T2 and T3 data were included for curve fitting. However, all E2, T2, and T3 data were corrected using the equations and slopes as used for the "regular" groups (i.e., T1 and E1).

also characterize E-MORB. E1-MORB Al_2O_3 and CaO/Al_2O_3 variations indicate that clinopyroxene joins the fractionating assemblage near ~5.5–6.0% MgO. FeO and TiO_2 plots show that oxides fractionated from E-MORB magmas with less than ~4.5% MgO.

[15] E2-MORB show the same relationships to E1-MORB as do T3-MORB relative to T1-MORB: they have lower CaO/Al_2O_3 as a result of both lower CaO and higher Al_2O_3 at a given MgO value, and significantly lower SiO_2. E2-MORB are among the least differentiated E-MORB. E2-MORB also tend to have slightly higher concentrations of incompatible oxides Na_2O, K_2O, TiO_2, and P_2O_5 than E1-MORB at the same MgO value.

[16] Samples from group 78D are scoriaceous: all glass with >60% vesicularity. Group 78D, with 6.15% MgO, is classified as an E2-MORB on the basis of its low SiO_2 content and high values of Na_2O, K_2O, TiO_2, and P_2O_5 relative to E1-MORB (Figure 4). This sample group has CaO and Al_2O_3 compositions that are more similar to E1-MORB, but H_2O content (0.18%) that is much lower than E1- or E2-MORB, indicating that it is degassed, consistent with its high vesicle content.

[17] H_2O contents of GSC samples correlate positively with K_2O contents (Figure 5b), indicating that H_2O behaves incompatibly, with H_2O slightly more compatible than K_2O (i.e., bulk distribution coefficient (D) for $H_2O > D$ for K_2O). This result is consistent with the conclusions of *Michael* [1988, 1995], *Dixon et al.* [1988], and *Danyushevsky et al.* [2000], who argued that water in basalts behaves incompatibly during melting and crystallization, with a D of ~0.01. The strong positive correlation between K_2O and H_2O suggests that the same processes that affect abundances of other incompatible elements in MORB also control H_2O. Additionally, this excellent correlation is consistent with negligible contamination of the magmas by seawater, which should elevate H_2O relative to K_2O in a nonsystematic way [*Danyushevsky et al.*, 2000].

3.3. $MgO_{8.0}$ Calculations

[18] In order to determine parental magma compositions for each magma type, we have adjusted our data for the effects of low-pressure differentiation by calculating oxide values at MgO = 8.0% [*Klein and Langmuir*, 1987]. The adjusted values are indicated hereafter with a subscript of 8.0. This adjustment allows for comparisons among lava types as well as with global MORB data sets. We used least squares regressions to quantify the oxide variations versus MgO for each type and adjusted all data using the slope of the regression. Samples with MgO contents >8.5% or <3.5% were excluded; thus the empirical lines along which we adjusted the data probably represent cotectic crystallization of olivine and plagioclase ± pyroxene only. Separate slopes were calculated for each of the three general magma types (i.e., N-, T1- and E1-MORB). Straight lines were fitted through SiO_2, Al_2O_3, FeO*, and CaO data. Observed trends for the minor elements K_2O, Na_2O, TiO_2, P_2O_5, and H_2O are curved, as expected for incompatible elements approximating Henry's Law behavior; accordingly, best-fit power law curves were used for adjusting these data.

[19] Regression of the E2-MORB data alone would not produce a statistically valid regression due to the small number of data points. We therefore adjusted E2-MORB using the same slope as for E1-MORB, assuming that they evolved by similar processes, but from a different parental magma. Similarly, T2- and T3-MORB were excluded from

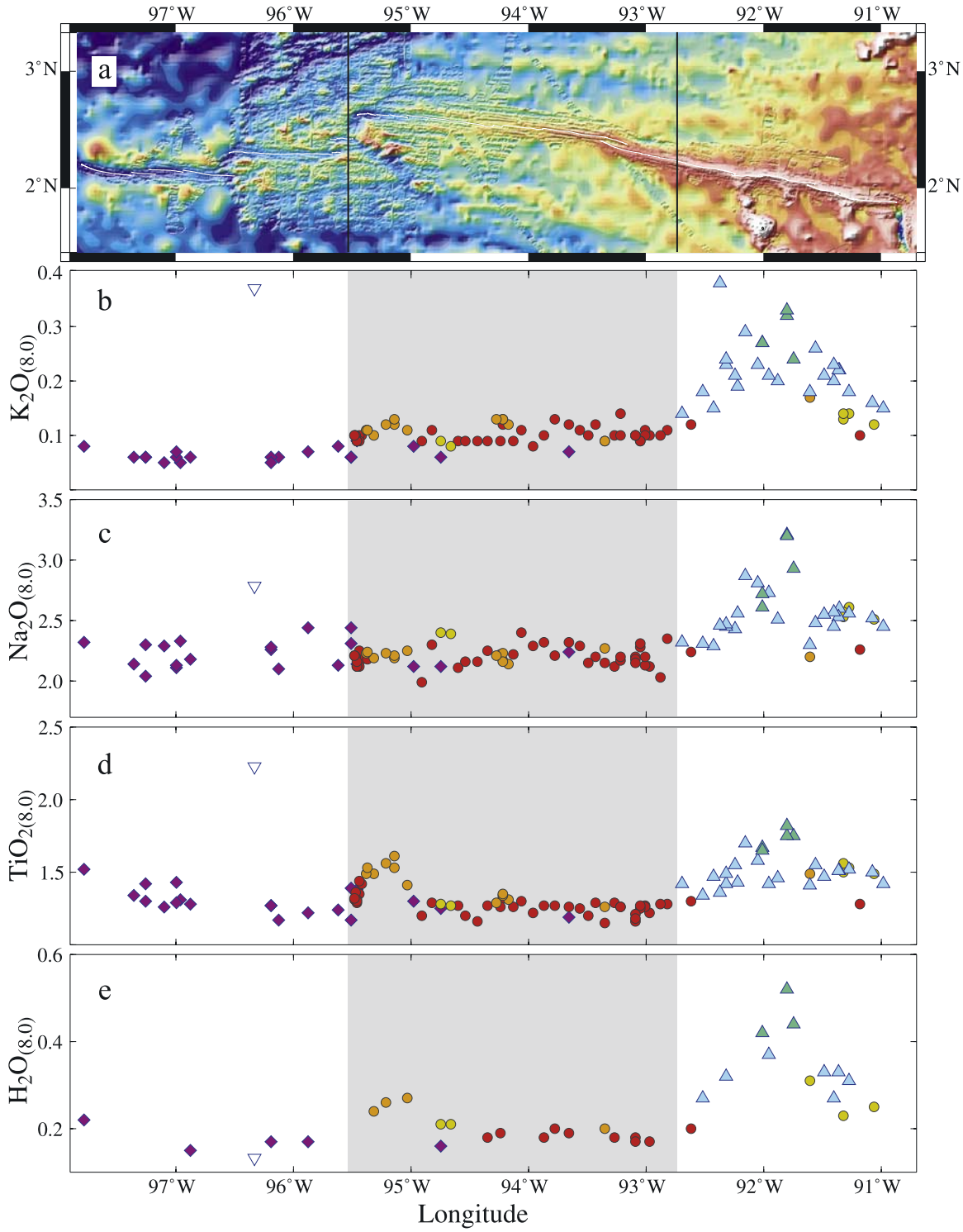

Figure 6. Along-axis compositional variations. Bathymetric map (Figure 6a) is included at the same longitudinal scale to show ridge features that correspond with compositions. Figures 6b–6e and Figures 6g–6i are fractionation-adjusted compositions. The gray shaded boxes delineate the three major provinces, defined by correlated geochemical, geophysical, and bathymetric characteristics [*Detrick et al.*, 2002]. Open symbols in Figure 6f indicate samples with anomalously high K/Ti ratios created by fractionation of Ti-bearing oxides, not elevated K_2O contents.

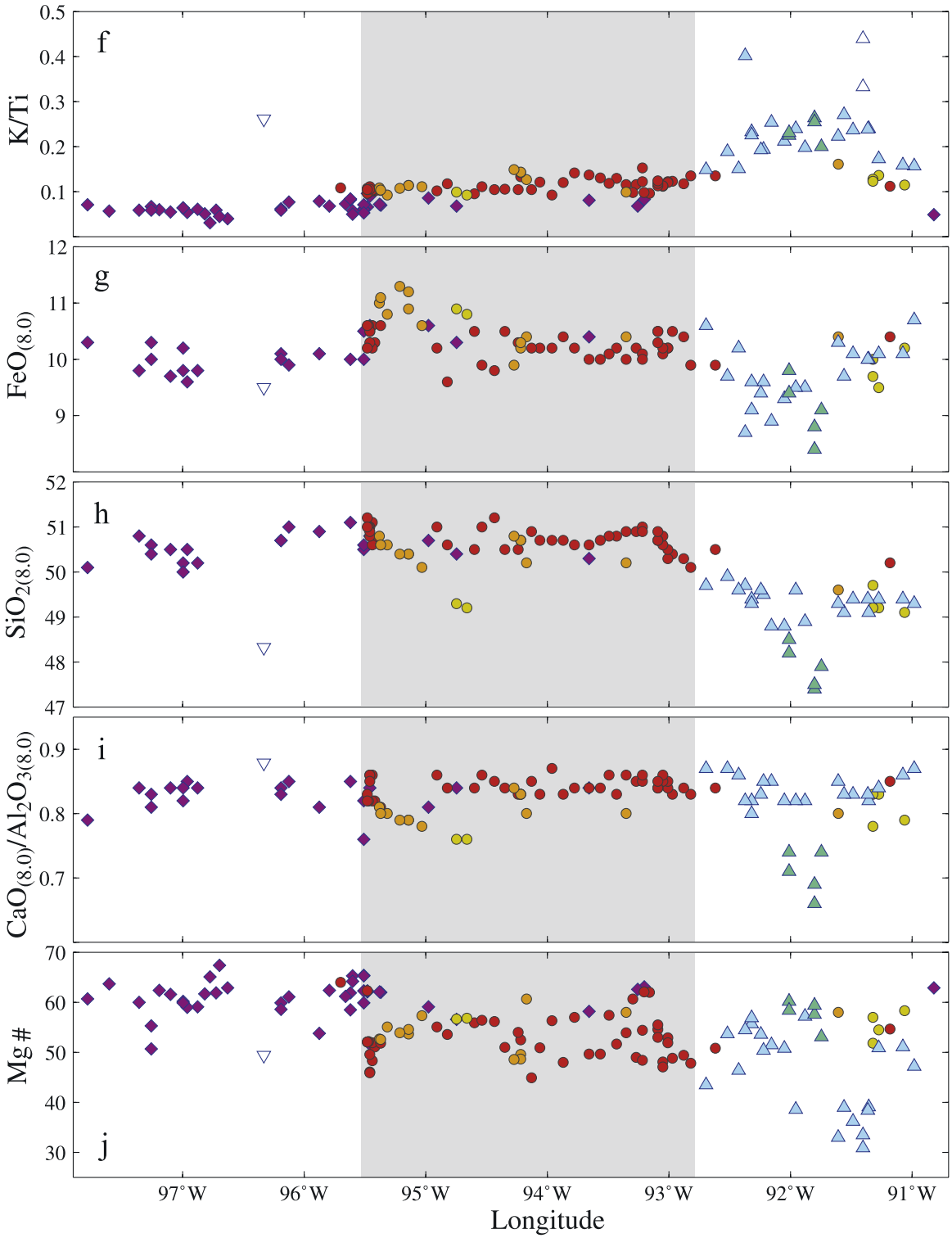

Figure 6. (continued)

the regressions, but oxide values were adjusted using the same slope as used for T1-MORB. Slopes determined in this study are given in Table 3.

3.4. Along-Axis Variations

[20] E-MORB dominate the GSC east of 92.6°W; T-MORB are mainly found between 92.6°W and 95.5°W (shaded area in Figures 6a–6j); only N-MORB (except for the 78D scoria E2-MORB) are found west of 95.7°W. The limit of E-MORB occurrence is consistent with the ''plume-influenced'' ''type B'' basalts of *Fisk et al* [1982]. *Fisk et al.* [1982] and *Schilling et al.* [1982] also noted petrological differences between basalts from within the ''H-zone'' (high magnetic amplitude zone [*Anderson et al.*, 1975]), which is confined to the region of the GSC between the tips of the propagating rifts at 95.5°W and 85°W, and those outside of it. The boundary separating N-MORB- and T-MORB-dominated provinces in our data coincides with the 95.5°W propagating rift tip (Figure 6a).

[21] The western limit of the E-MORB-dominated province near 92.7°W, coincides with the transition from an axial high morphology (to the east) and the rapid doubling of the depth to the seismically imaged axial magma lens and base of layer 2A (from east to west) [*Detrick et al.*, 2002]. The westernmost extent of T-MORB, 95.7°W, corresponds with the propagating rift (PR) system near 95.5°W. This PR tip marks the boundary between axial rift-valley morphology, to the west, and the region between 95.5°W and 92.7°W, dominated by transitional morphology.

[22] Within the N-MORB region, $FeO^*_{(8.0)}$ and $TiO_{2(8.0)}$ decrease slightly from west to east, while $SiO_{2(8.0)}$ increases. Between ~95.1°W and 95.5°W, $FeO^*_{(8.0)}$ and $TiO_{2(8.0)}$ are elevated relative to the surrounding regions [*Christie and Sinton*, 1981, 1986; *Sinton et al.*, 1983]; $H_2O_{(8.0)}$ also is high in this region. From ~94.2°W to the propagating rift tip near 95.5°W, Mg# (molar MgO/(MgO + FeO*)) shows a well-defined trend, decreasing to the west. Between ~94.2°W and the eastern edge of the overlapping spreading center system at ~93.2°W, $FeO^*_{(8.0)}$ and $SiO_{2(8.0)}$ are nearly constant, while Mg# is highly variable compared to its narrow range at any given location farther to the west. East of ~93.1°W, T-MORB $FeO^*_{(8.0)}$ and $SiO_{2(8.0)}$ values decrease. These trends continue beyond the first occurrence of E-MORB at 92.7°W until they reach their minima near 91.7°W.

[23] Along-axis variations in elements adjusted to 8.0% MgO show that the most extreme values are between ~91.7°W and 92.4°W (Figures 6a–6j). $K_2O_{(8.0)}$, $TiO_{2(8.0)}$, $Al_2O_{3(8.0)}$, $Na_2O_{(8.0)}$, $P_2O_{5(8.0)}$, and $H_2O_{(8.0)}$ peak in this region, while $FeO^*_{(8.0)}$, $SiO_{2\ (8.0)}$, $CaO_{(8.0)}$, and $CaO_{(8.0)}/Al_2O_{3(8.0)}$ are at their lowest values. We infer that these geochemical features characterize the most plume-influenced rocks.

[24] Samples from dredge 17, at 91.8°W, have the highest $TiO_{2(8.0)}$, $Al_2O_{3(8.0)}$, $Na_2O_{(8.0)}$, and $P_2O_{5(8.0)}$, and the lowest $FeO^*_{(8.0)}$, $SiO_{2(8.0)}$, and $CaO_{(8.0)}/Al_2O_{3(8.0)}$, thus defining the location of greatest plume influence along the western GSC. We note that the apparent peaks in K/Ti near 91.4°W (samples 11D-a and 11D-b, Figure 6f) probably reflect peaks in fractionation (MgO contents of 3.33 and 3.98%, respectively) rather than peaks in parental magma. The parental magma peak in K/Ti is therefore farther west, which is in agreement with the extremes in the other oxides. The greatest geochemical signature of plume influence also coincides with the greatest crustal thickness (~8 km) [*Canales et al.*, 2002].

4. Modeling Hydrous Melting

[25] Compared to N-MORB, E-MORB are enriched in oxides that are incompatible during melting of mantle peridotite (e.g., K_2O, Na_2O, TiO_2, Al_2O_3, H_2O). As shown by *Schilling et al.* [1982], the relative enrichment is approximately inversely proportional to the bulk distribution coefficient (D) for melting of mantle peridotite, i.e., the most incompatible elements are the most enriched. This relationship suggests that variable melting processes are important in controlling the observed distribution along axis [*Fisk et al.*, 1982; *Schilling et al.*, 1982]. *Verma and Schilling* [1982] and *Verma et al.* [1983] showed that Sr and Nd isotope ratios also vary along axis, with the highest $^{87}Sr/^{86}Sr$ and lowest $^{143}Nd/^{144}Nd$ occurring at 91°–92°W. As argued by these authors, these results also require variation in the contribution of at least two mantle source components along axis, with the higher $^{87}Sr/^{86}Sr$ and lower $^{143}Nd/^{144}Nd$ source components increasing to the east.

[26] In addition to the incompatible trace element and isotopic variations are variations in SiO_2, Al_2O_3, FeO and CaO, all of which occupy principal lattice sites in the major mantle minerals olivine, pyroxenes, spinel, and garnet. As such,

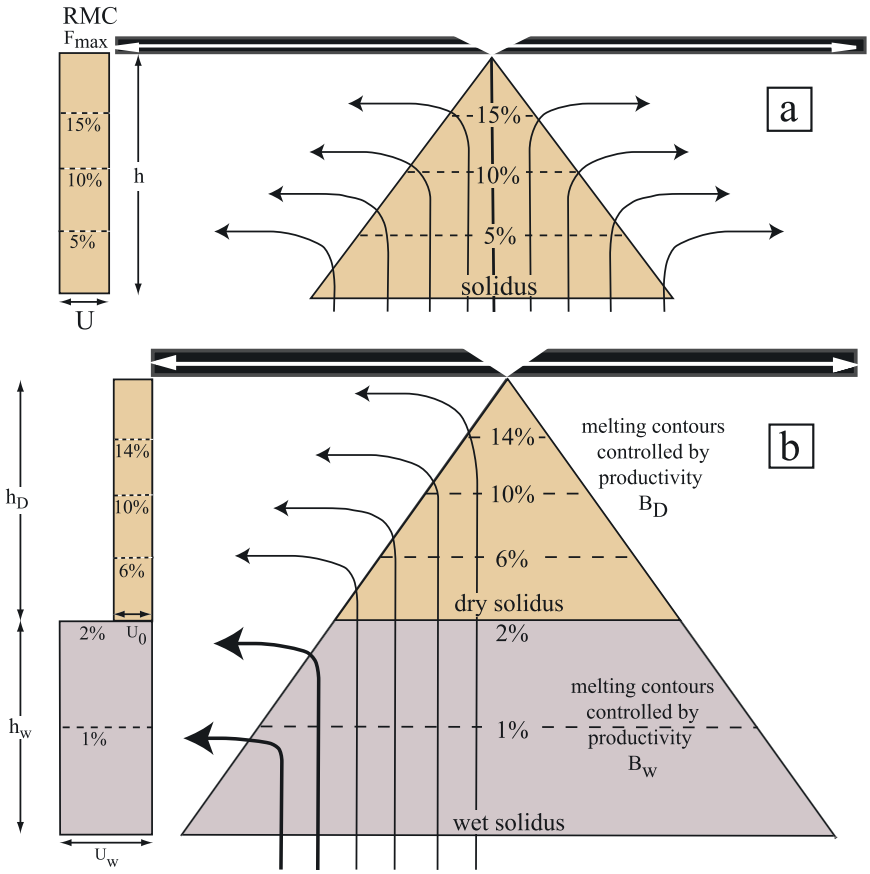

Figure 7. (a) Residual Melting Column (RMC) as illustrated by *Plank and Langmuir* [1992] and (b) modified to include an additional zone of hydrous melting that is created by the depression of the solidus when water is present in the mantle. The RMC is the net residue of melting. Black arrows indicate the rate solid mantle passes through and exits the melting zone to generate the RMC. Dashed contour lines indicate extent of melting in the melting region (triangular area) and extent of melt depletion in the RMC. (a) In an anhydrous melting region, contours are evenly spaced because productivity is assumed to be constant. h is the depth to the solidus. The width of the RMC is controlled by the flow rate of mantle material (U), which is assumed to be constant and equal to the spreading rate of the ridge. In this case, $\overline{F}$ is $^1/_2F_{max}$, enrichment of an element in the melt can be calculated from equation (3), and crustal thickness is simply the RMC area multiplied by $\overline{F}$. (b) Zone of hydrous melting with a height h_w (purple area) is now below the anhydrous zone (height h_D). Plume-driven flow rate through the hydrous region (U_w) may be the same as, or higher than, flow rate through the anhydrous region (U_0), as indicated by the greater thickness of the arrows. Productivity in the hydrous region (B_w) is probably lower than productivity in the anhydrous region (B_D) (see text). Depth to the dry solidus is here denoted as h_D; additional depth to the hydrous solidus is h_w; and the total depth of melting is $h_D + h_w$. In this case, mean melt fraction ($\overline{F}$) and melt composition (equations (12) and (10), respectively) take into account contributions from both the hydrous and anhydrous melting regions.

variations in these oxides are more likely to be controlled by stoichiometry during melting than by source enrichment. It is notable that many of the chemical characteristics of the most plume-influenced portion of the GSC are consistent with relatively low extents of partial melting. For example, E-MORB are enriched in incompatible elements, and this enrichment is coupled to high Al_2O_3 and low SiO_2 and CaO/Al_2O_3. The E-MORB lavas, which carry the strongest signature of relatively low extents of melting, are, however, found in the region of shallowest depths and greatest crustal thickness [*Detrick et al.*, 2002] and are nearest to the Galapagos "hot spot." Recent studies [e.g., *Plank and Langmuir*, 1992; *Detrick et al.*, 2002; *Asimow and Langmuir*, 2003; *Asimow et al.*, 2004] suggest that a key to understanding the apparent paradox (maximum melt production (thickest crust) coinciding with low mean extents of melting) is in the role of water on the melting of

upwelling mantle peridotite. For example, *Asimow and Langmuir* [2003] showed that the observed increase in crustal thickness close to the Galápagos hot spot can be associated with ~40% reduction in mean degree of melting when water is incorporated into mantle melting models.

[27] By depressing the solidus [*Kushiro*, 1968], the presence of water in the mantle increases the depth at which melting begins, and expands the volume of mantle undergoing melting [*Schilling et al.*, 1980; *Plank and Langmuir*, 1992] (Figure 7). The total melt volume therefore includes a contribution from anhydrous melting, plus a contribution from an additional volume of mantle undergoing hydrous melting. Because the extent of melting within the hydrous melting zone is likely to be low [*Hirth and Kohlstedt*, 1996; *Hirschmann et al.*, 1999; *Braun et al.*, 2000; *Asimow and Langmuir*, 2003; *Katz et al.*, 2003; *Asimow et al.*, 2004], this "extra" source volume can contribute melt with a high proportion of incompatible elements. The total area over which melting takes place and the total melt production are increased, but the mean extent of melting for the total melt volume may be reduced. *Gaetani and Grove* [1998] showed that elevated water content also affects the major element composition of a melt, tending to decrease SiO_2, FeO, MgO, and CaO. *Asimow and Langmuir* [2003] and *Asimow et al.* [2004] argued that low FeO in hydrous magmas is dominated by fractionation effects, rather than melting.

[28] The recognition of the potential importance of water to enhancing melt production was first noted for the Galápagos region by *Schilling et al.* [1982] and *Fisk et al.* [1982] and for the region around the Azores hot spot [*Schilling et al.*, 1980; *Bonatti*, 1990; *Asimow et al.*, 2004]]. *Asimow and Langmuir* [2003] developed quantitative models that relate source composition, including water content, to melting processes along the GSC using previously published data as constraints. This work indicated that hydrous melting can explain many of the compositional and crustal thickness variations of the region and that potential temperatures along the hot spot-affected ridge are less than those predicted from anhydrous models. In the following sections, we develop an alternative hydrous melting model that allows for variable extents of active upwelling in the hydrous and anhydrous melting regions. The results of this modeling support the general conclusions of *Asimow and Langmuir* [2003], with important differences in the required compositional and temperature variations along axis.

4.1. Theory

[29] *Plank and Langmuir* [1992] (hereafter PL92) evaluated the effects of melting and mixing melts on crustal composition by examining the residual melting column (RMC, Figure 7a), the conceptual "net result" of melting of the mantle [see *Langmuir et al.*, 1992; PL92]. The RMC is useful for calculating the volume and composition of the aggregate melt that makes up the oceanic crust, somewhat independent of the physical shape of the melting region.

[30] When the rate of mantle flowing through and exiting the melting region is constant over the depth of the melting zone, the width of the RMC is constant and the mean concentration ($\overline{C_L}$) of a given element in the melt arising out of the RMC is

$$\overline{C_L} = \frac{\int_0^{F\max} F[C_L(F)]dF}{\int_0^{F\max} FdF}, \quad (1)$$

where F is melt fraction. The quantities $\overline{C_L}$ and F are related by a melting function, $C_L(F)$. PL92, for example, used the accumulated fractional melting (AFM) equation [*Shaw*, 1970],

$$C_L/C_0 = \frac{1-(1-F)^{1/D}}{F}, \quad (2)$$

where D is the bulk solid/liquid partition coefficient of the element being evaluated, C_0 is the initial source concentration of that element, and fractional melts are pooled between melt fractions 0 and F.

[31] Substituting equation (2) into equation (1) and integrating yields the "pooled melting" equation:

$$\overline{C_L}/C_0 = \frac{F_{\max} + \frac{(1-F_{\max})^{1/D+1}-1}{1/D+1}}{\frac{F_{\max}^2}{2}}. \quad (3)$$

[32] The mean fraction of melting, $\overline{F}$, is the total quantity of melt divided by the height of the melting zone,

$$\overline{F} = \frac{\int_{h_D}^{0} F(z)dz}{\int_{h_D}^{0} dz}, \quad (4)$$

where z is depth below the top of the melting zone, dz is an infinitely small depth interval, and melting begins at $z = h_D$. Melt productivity, B, is dF/dz. If it is uniform with depth, $F(z) = Bz$, $B = F_{\max}/h_D$, and

$$\overline{F} = \frac{\int_{h_D}^{0} Bz dz}{\int_{h_D}^{0} dz} = \frac{1}{2} F_{\max}, \quad (5)$$

where $F_{\max}$ is the maximum extent of melting at the top of the RMC. Crustal thickness, Z_{cr}, which is proportional to the total volume of melt extracted from the melting region, is calculated simply by multiplying $\overline{F}$ by h_D, the depth to the solidus.

[33] Equations (3) and (5) correspond with PL92 equations (7) and (8), respectively. These equations are based on four assumptions: flow rate through and out of the melting zone that is uniform with depth (i.e., RMC of uniform thickness), adiabatic melting, perfect fractional melting, and constant melt productivity.

[34] In Figure 7b, we relax the assumptions of uniform mantle flow and constant melt productivity (Figure 7b). In this case, the RMC width is controlled by $U(z)$, the rate of flow through and out of the melting region. The mass flux of melt removed at a given depth is proportional to $U(z)F(z)dz$, the mass flux of a given element is proportional to $C_L(z)U(z)F(z)dz$, and therefore adding all melt concentrations from all depths in the RMC yields

$$\overline{C_L} = \frac{\int_{h_W+h_D}^{0} U(z)F(z)C_L(z)dz}{\int_{h_W+h_D}^{0} U(z)F(z)dz}. \quad (6)$$

We greatly simplify the rather complex change in melting behavior as a function of pressure by separating the melting zone into two regions: an anhydrous melting zone spanning depths of $z = 0 - h_D$, and a hydrous zone with $z = h_D - h_w$. We approximate the change in melting behavior between the two zones by specifying constant but distinct average productivities, B_w and B_D, for the hydrous and dry melting zones, respectively (Figure 7).

[35] Equation (6) also allows us to treat a more complex mantle flow function $U(z)$ associated with plume-ridge interaction. For a normal mid-ocean ridge where mantle flow is passively driven by plate separation, $U(z)$ is nearly constant (i.e., approximately the half spreading rate of the ridge) and therefore this term drops out of (6). The flow rate of a mantle plume beneath the lithosphere, however, is likely to vary as a strong function of depth [e.g., *Ito and Mahoney*, 2002; *Ribe et al.*, 1995; *Ito et al.*, 1999]. Deep in the upper mantle, the buoyant mantle plume stem rises rapidly, possibly an order of magnitude or more times typical plate motions [e.g., *Ito et al.*, 1999]. As it begins to interact with the lithosphere, the material ascends at a slower rate and is diverted sideways. Mantle plume buoyancy can thus push mantle rapidly into and out of the deep (hydrous) portion of the melting zone many times more rapidly than plate spreading can pull material in and out of the shallow (anhydrous) portion of the melting zone. Again, we simplify the continuous function of $U(z)$ by specifying an average velocity U_w through the hydrous zone and an average velocity U_0 through the anhydrous melting zone. If U_0 is approximately the half spreading rate of the two plates, then the fundamental parameter U_w/U_0 describes the speed of deep mantle plume flow relative to plate motion, with $U_w/U_0 = 1$ representing the condition beneath a normal mid-ocean ridge, and $U_w/U_0 > 1$ representing plume influence. Plume-driven flow ($U_w/U_0 > 1$) also contrasts with "active" mantle flow beneath mid-ocean ridges, which is predicted to be driven by the more shallow buoyancy associated with melting. This shallower, melt-related buoyancy enhances the flux of mantle though the shallow portion of the melting zone [*Scott and Stevenson*, 1989; *Turcotte and Morgan*, 1992] and thus could be simulated by $U_w/U_0 < 1$, but in this study, we examine only $U_w/U_0 \geq 1$.

[36] With these assumptions, an equation describing pooled melt concentrations,

$$\overline{C_L}/C_0 = \frac{\frac{1}{C_0}\left[\int_0^{F_w} \frac{U_w F C_L(F) dF}{B_w} + \int_{F_w}^{F\max} \frac{U_0 F C_L(F) dF}{B_D}\right]}{\int_0^{F_w} \frac{U_w F dF}{B_w} + \int_{F_w}^{F\max} \frac{U_0 F dF}{B_D}}, \quad (7)$$

has two parts. The first integral in the numerator represents melting in the hydrous zone to a maximum fraction F_w and the second integral in the numerator represents melting in the anhydrous region, which continues to $F_{\max}$. With

$$B_w = \frac{F_w}{h_w} \quad (8)$$

$$B_D = \frac{F_{\max} - F_w}{h_D}, \quad (9)$$

and using the AFM function (2) to relate C_L to F, we integrate equation (7) and get our "hydrous melting equation,"

$$\overline{C_L}/C_0 = \left\{ \frac{U_w}{U_0}\frac{h_w}{F_w}\left[F_w + \frac{(1-F_w)^{1/D+1}-1}{1/D+1}\right] + \frac{h_D}{F_{\max}-F_w}\left[F_{\max}-F_w + \frac{(1-F_{\max})^{1/D+1}-(1-F_w)^{1/D+1}}{1/D+1}\right]\right\} \Bigg/ \left\{\frac{U_w}{U_0}\frac{F_w h_w}{2} + \frac{h_D(F_{\max}+F_w)}{2}\right\} \quad (10)$$

[37] The denominator of equation (10) is proportional to crustal thickness (Z_{cr}), with the first and second terms representing contributions to the crust by hydrous melting and anhydrous melting, respectively. Seismically constrained values of Z_{cr} [*Canales et al.*, 2002] can be incorporated into (10) by substituting

$$F_{\max} = \frac{2\left[\left(\frac{\rho_c}{\rho_m}Z_{cr}\right) - \frac{U_w}{U_0}\frac{F_w h_w}{2}\right]}{h_D} - F_w, \quad (11)$$

where the ratio of crustal density (ρ_c) to mantle density (ρ_m) converts weight fraction to volume fraction.

[38] Finally, the mean degree of melting, $\overline{F}$, is the weighted average of the mean degree of melting in the hydrous and anhydrous regions,

$$\overline{F} = \frac{\int_{h_W+h_D}^{0} U(z)F(z)dz}{\int_{h_W+h_D}^{0} U(z)dz} = \frac{\frac{U_w}{U_0}\frac{F_w h_w}{2} + \frac{h_D(F_{\max}+F_w)}{2}}{\frac{U_w}{U_0}h_w + h_D}. \quad (12)$$

Note that if $F_w = h_w = 0$ and $U_w/U_0 = 1$, equation (12) reduces to equation (5), and equation (10) reduces to equation (3).

4.2. General Predictions of the Hydrous Melting Model

[39] Figure 8 demonstrates the effects of hydrous melting and plume-driven flow (equation (10)) compared to "dry" melting and uniform flow (equation (3)). As h_w increases with increasing concentrations of H_2O in the mantle source, $\overline{F}$ decreases (Figure 8a), reflecting the contribution from a relatively large volume of mantle melting to only small degrees. The plume-driven flow param-

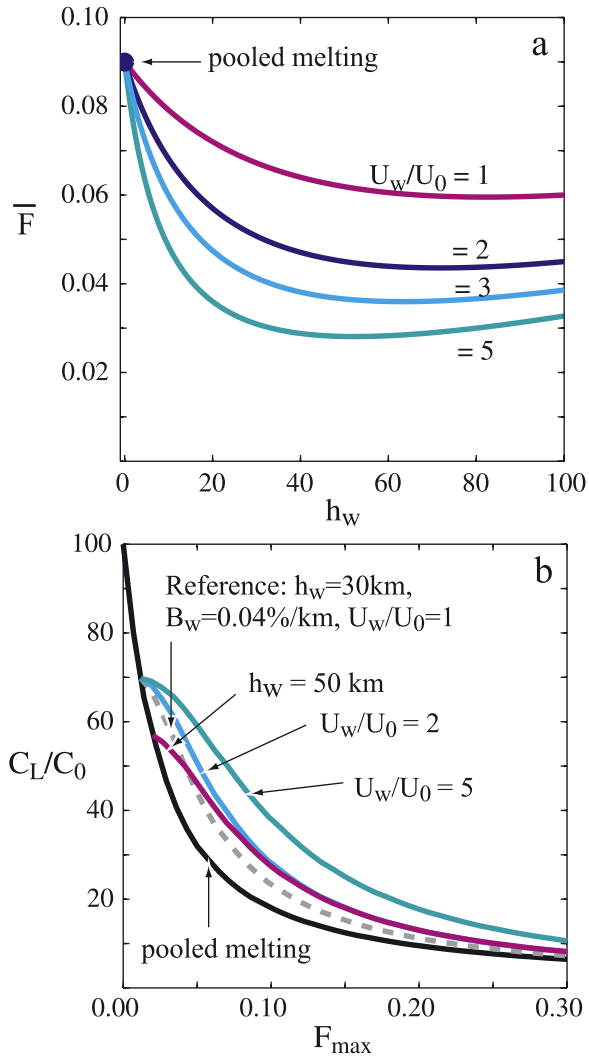

Figure 8. General solutions to the hydrous melting equation. (a) Effects of variable upwelling rates on mean degree of melting using the hydrous melting equation (equation (10)) (curves) compared to the $\overline{F}$ solution using the anhydrous pooled melting equation (equation (3)) (blue dot). All calculations are for a melting region with constant depth to the dry solidus (h_D = 50 km) and constant melt productivity in the dry region (B_D = 0.36%/km). Hydrous solutions use B_w = 0.045%/km. The effects of variable upwelling rate (U_w/U_0 = 1–5) are shown; higher upwelling rates produce lower $\overline{F}$ values at a given h_w. (b) Effects of h_w, U_w/U_0, and B_w on incompatible element enrichment (relative to the source) at various degrees of melting. The solid black line is C_L/C_0 predicted by the pooled melting equation (equation (3)) of *Plank and Langmuir* [1992] for an element with D = 0.01; all other lines are predictions based on the hydrous melting equation for an element with D = 0.01. The gray dashed line is a reference model with midrange values of h_w (30 km), B_w (0.04%/km), and U_w/U_0(1). All other lines have the same values for two of the variables, and the third variable has been changed as noted.

eter, U_w/U_0 also controls the flux of material melting in the hydrous region. Increasing U_w/U_0 leads to decreases in $\overline{F}$ at the same value of h_w (Figure 8a).

[40] Figure 8b shows the effects of h_w and U_w/U_0 on the enrichment of an incompatible element (D = 0.01 shown) in a melt, compared to that predicted by the equation for anhydrous, uniform mantle flow (equation (3)). When melting is only occurring in the hydrous region, $F_{\max} \leq F_w$ and C_L/C_0 follows the same curve for all conditions, including anhydrous melting. As soon as productivity increases at the onset of dry melting, the predicted curves diverge. For hydrous plus anhydrous melting, a proportionally smaller flux of depleted melts is diluting the hydrous melts and C_L/C_0 remains higher than the curve for anhydrous melting only. Melt enrichment (C_L/C_0) increases with increasing hydrous melting interval h_w and flow parameter U_w/U_0 because both of these parameters increase the relative flux of hydrous (low-degree) melting. For example, compared to reference values of h_w = 30 km and U_w/U_0 = 1, approximately doubling h_w (h_w = 50 km, U_w/U_0 = 1) has approximately the same effect of doubling U_w/U_0 (h_w = 30 km, U_w/U_0 = 2), both increasing C_L/C_0 by ~15% at $F_{\max}$ = 0.2. Increasing U_w/U_0 to 5 approximately doubles C_L/C_0 at $F_{\max}$ = 0.2. These general calculations illustrate the importance of hydrous melting and plume-driven flow on the amount melts are enriched relative to the initial source. As we demonstrate next, it is thus necessary to consider these factors when using observed variations in magma compositions to constrain source variations.

4.3. Application to G′ Data

[41] Although isotopic data [e.g., *Schilling et al.*, 2003] suggest that there may be quasi-continuous variation in source composition along axis, major and minor element glass data indicate that the western GSC can be divided into three broad regions respectively dominated by N-, T-, and E-MORB. In this study we use compositional data that are the average fractionation-corrected compositions for lavas from these three regions. Because the processes controlling major element oxides such as SiO_2, CaO, Al_2O_3, and FeO* are not easily accounted for by simple distribution coefficients, we focus only on the incompatible components K, Na_2O, Ti, and H_2O. The behavior of these elements during melting is moderately well known [e.g., *Dixon et al.*, 1988; *Johnson et al.*, 1990; *Langmuir et al.*, 1992; *Michael*, 1995; *Niu et al.*, 1996]. Although partitioning relations can be expected to vary with changing temperature, pressure and composition, there are too few detailed data to allow for a fully quantitative treatment of these effects. We have therefore adopted the common approach of using constant D values throughout the melting process (Table 4).

[42] In the hydrous melting equation (equation (10)), C_L is controlled by the independent variables D, $F_{\max}$, B_D, h_D, B_w, h_w, C_0, U_w/U_0, and Z_{cr} (with equation (11)). The average values of Z_{cr} for each portion of the ridge, and the average values of $K_{(8.0)}$, $H_2O_{(8.0)}$, $Na_2O_{(8.0)}$, and Ti $_{(8.0)}$ are input into our model as constant, singular variables for each general MORB type (Table 4). For melt productivities, we consider B_D values of 0.26–0.53%/km (0.8–1.6%/kbar). This range of productivities fully encompasses the values used by *Langmuir et al.* [1992] and *McKenzie and Bickle* [1988], and is consistent with average productivities in the anhydrous region shown by *Asimow et al.* [2001]. We considered a range of B_w values between 0.03–0.05%/km (0.09–0.15%/kbar), which we estimated from curves of *Asimow et al.* [2001, 2004].

[43] Water concentration in the source (C_0^{H2O}) and the height of the wet melting column (h_w) are linked, but the precise relationship is not yet well understood. *Hirth and Kohlstedt* [1996] schematically related the depression of the hydrous solidus to depth (and pressure) on the basis of calculated contours of the activity of water in olivine. *Bell et al.* [2003] asserted that due to errors in calibration, all estimations of water solubility in olivine to date are underestimates and require upward revision by a factor of 2–4. *Katz et al.* [2003], *Asimow and Langmuir* [2003], and *Asimow et al.* [2004] incorporate nonlinear dependences of h_w on C_0^{H2O}. The parameterization of *Katz et al.* [2003] predicts an increase of h_w due to an increase in water content of ~0.10 ± 0.03 km/ppm at C_0^{H2O} = 550 ppm, whereas the dependence along the adiabats of *Asimow et al.* [2004] decreases from approximately 0.42 km/ppm at C_0^{H2O} = 50 ppm to ~0.19 km/ppm at C_0^{H2O} = 300 ppm. In a later section we will show that G′ data are consistent with C_0^{H2O} values <~250 ppm. Thus a simplified linear relation

$$h_w = (0.25 \pm 0.01) C_0^{H2O}, \quad (13)$$

Table 4. Variables Used in Model

Variable	Description	Constraints	Range Allowed	Grid Search Step Size
Z_{cr}	observed crustal thickness, (km)	reflection/refraction experiments [*Canales et al.*, 2002]	N-MORB: 5.7 (W. of 95.5°W) T-MORB: 6.3 (92.7–95.5°W) E-MORB: 7.5 (E. of 92.7°W)	
C^i_{Lobs}	fractionation-corrected concentration of element i in glass, averaged for each MORB type (ppm)	backtracking of geochemical data to magma composition at 8.0 wt% MgO	N-MORB K: 500, H_2O: 1600, Na_2O: 2.15, Ti: 7200 T-MORB K: 750, H_2O: 1600, Na_2O: 2.15, Ti: 7200 E-MORB K: 1575, H_2O: 2800, Na_2O: 2.45, Ti: 9900	
D	bulk distribution coefficients	estimated from *Dixon et al.* [1988]; *Johnson et al.* [1990]; *Langmuir et al.* [1992]; *Michael* [1995]; *Niu et al.* [1996]	K: 0.0024, H_2O: 0.01, Na_2O: 0.03, Ti: 0.08	
$C_0^{Na\ a}$	initial concentration of Na in source (ppm)		sufficient to encompass the possible solutions, generally 1000–3000 ppm	100 ppm
U_w/U_0	flow rate of material out of hydrous melting region normalized by flow (spreading) rate out of anhydrous region		N-MORB: 1–2 T-MORB: 1–10 E-MORB: 1–10	0.2 0.5 0.5
h_w	depth from anhydrous solidus to volatile-present solidus (km)		N-MORB: 0–46 km T-MORB: 0–50 km E-MORB: 0–74 km	2 km
h_D	depth to dry solidus (km)		1–100 km	0.5 km
B_w	productivity dF/dz in wet melting region (km^{-1})	estimates of averages in low-productivity melting regions [*Asimow et al.*, 2001]	0.0003 to 0.0005 km^{-1} (0.08–0.16%/kbar)	0.0001 km^{-1}
B_D	productivity dF/dz in dry melting region (km^{-1})	averages in high-productivity region of melting [*Asimow et al.*, 2001]	0.0027–0.0053 km^{-1} (0.8–1.6%/kbar)	
h_w/C_0^{H2O}	relationship between water content in mantle and the depression of the solidus (km/ppm)	*Hirth and Kohlstedt* [1996]; *Bell et al.* [2003]; *Asimow et al.* [2004]. See text for discussion.	0.24–0.26 km/ppm	
$C^i_{L\ pred}$	predicted concentration of element i in parental magma (ppm)			
C_0^i	initial concentration of element i in source (ppm)			
F	mean fraction of melting			
F_{max}	maximum degree of melting in entire melting region	relates to Z_{cr} through equation (11)		
F_w	maximum degree of hydrous melting			

[a] The computational procedure involves searching through possible values of C_0^{Na}. Search through C_0^{Na} is arbitrary; searching through the source composition of any other element yields identical solutions.

with h_w in km and C_0^{H2O} in ppm, is a reasonable approximation to the solidus depression at relatively low water contents.

[44] For each MORB type, we have seven equations: equations (8), (9), (11), and (10) for $K_{8.0}$, $H_2O_{8.0}$, $Na_2O_{8.0}$, and Ti $_{(8.0)}$, plus constraints on an eighth equation (equation (13)). It is thus possible to place bounds on eight unknowns: F_{max}, h_D, h_w, U_w/U_0, and four C_0s. We use a grid search method to invert for the range of solutions that satisfy data on C_L and Z_{cr}, given ranges of B_D, B_w, and h_w/C_0^{H2O}.

4.4. Relation to Previous Hydrous Melting Models

[45] Various methods have been developed that use geochemical data to understand the partial melting process. Like us, *McKenzie and O'Nions* [1991] use an inverse method, but their method differs in that it assumes a source composition and uniform mantle flow (U_w/U_0 = 1) to invert for F as a function of depth (i.e., effectively inverting for F_{max}, h_D, and B_D). *Maclennan et al.* [2001] built upon *McKenzie and O'Nions* [1991] to also invert for $U(z)$. Both *McKenzie and O'Nions* [1991] and *Maclennan et al.* [2001] only considered anhydrous melting and neither uses crustal thickness directly in the inversion. In contrast, the forward methods of *Katz et al.* [2003] and *Asimow and Langmuir* [2003] explicitly incorporate the effects of water, consistent with thermodynamic constraints calibrated against available experimental data on peridotite melting, solubility relations and hydrous equilibria. These models also allow for continuous variation in productivity with depth and water content as well as for variations in modal mineralogy of the source as melting proceeds. As such, these models represent the most realistic models of peridotite melting in the presence of water that are currently available. Such models present many advantages. The principal disadvantages are that many of the dependencies in these models are poorly constrained by currently available experimental data and the models are computationally complex.

[46] Our more rudimentary treatment of hydrous melting is based on analytic solutions of basic principles of mass balance and phase equilibria; it is relatively simple computationally and extremely flexible. It allows several variables to vary independently, even when we suspect that there should be dependencies among some of them (e.g., B_w and C_0^{H2O} [*Asimow et al.*, 2004]). This allows us to produce a broad range of solutions that can then be evaluated for reasonableness as our understanding of the different dependencies improves. The most important weakness of our method is that we must prescribe a range of productivities and h_w/C_0^{H2O}, and thus can only place approximate bounds on possible solutions. One obvious strength is that we can place bounds on all the unknowns, including source composition (i.e., C_0s). A unique feature of our model is

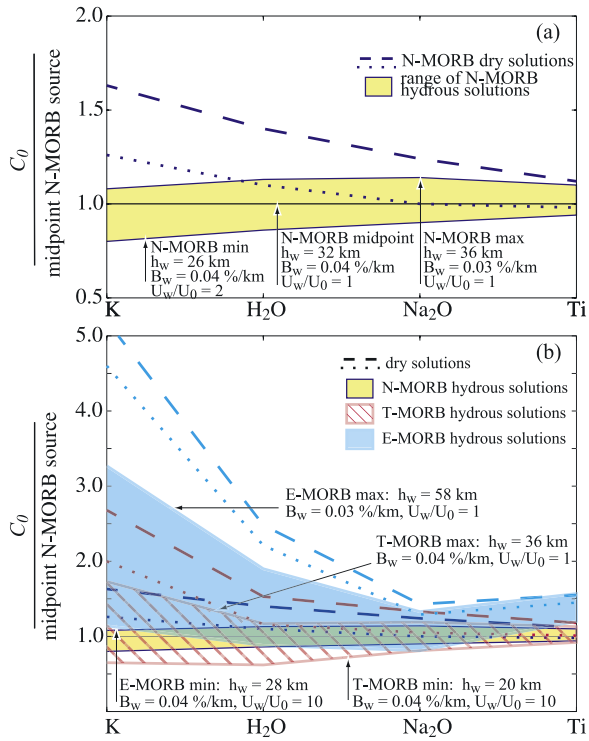

Figure 9. N-MORB mantle-normalized diagram showing relative range of source concentrations required to match the average fractionation-corrected compositions and crustal thickness for (a) N-MORBs and (b) N-, T-, and E-MORBs. Concentrations are normalized by a "midpoint" N-MORB composition, chosen because the variables h_w, B_w, and C_0^{Na} are near the median of the values for which reasonable solutions were produced. Passive upwelling, U_w/U_0 = 1, is used to calculate this midpoint. See Table 5 for associated parameters. Dashed and dotted lines show the maximum and minimum concentrations, respectively, required for each MORB type assuming only anhydrous melting. Shaded regions show the range of hydrous melting solutions for each MORB type. N-MORB hydrous solutions are shown in yellow; T-MORB solutions are shown with red stripes; and E-MORB solutions are shown in light blue. Compared to dry melting, hydrous melting requires lower source concentrations of incompatible elements to explain G′ data for all MORB types.

Table 5. Range of Model Inputs That Combine to Match G′ Data[a]

	C_0^K, ppm	C_0^{H2O}, ppm	C_0^{Na2O}, ppm	C_0^{Ti}, ppm	B_w, %/km	h_w, km	F_w fraction	B_D, %/km	h_D, km	F fraction	F_{max} fraction	U_w/U_0
						N-MORB						
Dry1[b]	41	136	2100	991	0	0	0	0.2643	60.5	0.080	0.160	1
Dry2	53	175	2600	1136	0	0	0	0.4473	46.5	0.104	0.208	1
min[c]	26	107	1900	955	0.04	26	0.010	0.2746	54.0	0.046	0.159	2
max	35	141	2400	1113	0.03	36	0.011	0.4870	41.5	0.062	0.213	1
midpoint[d]	32	124	2100	1012	0.04	32	0.013	0.3336	49.0	0.060	0.176	1
						T-MORB						
Dry1	65	144	2200	1020	0	0	0	0.2694	63.0	0.085	0.170	1
Dry2	86	190	2800	1197	0	0	0	0.4840	47.0	0.114	0.227	1
min	21	77	1700	934	0.04	20	0.008	0.3387	49.5	0.021	0.176	10
max	56	146	2500	1148	0.04	36	0.014	0.5081	42.0	0.069	0.228	1
						E-MORB						
Dry1	148	275	2700	1469	0	0	0	0.2712	68.5	0.093	0.186	1
Dry2	168	309	3000	1572	0	0	0	0.3477	60.5	0.105	0.210	1
min	37	110	1700	1211	0.04	28	0.011	0.3181	51.5	0.019	0.175	10
max	105	237	2800	1591	0.03	58	0.017	0.5013	45.0	0.062	0.243	1

[a] Solutions listed produce magma compositions that match G′ crustal thickness and composition values from Table 4. These maximum and minimum values, normalized to the N-MORB midpoint value, were used to plot Figure 9. Symbols are explained in Table 5 and text.
[b] Dry solutions are the minimum (Dry1) and maximum (Dry2) of all solutions predicted by the anhydrous pooled melting equation (equation (3)) that fit our inputs and constraints. All variables that were used to create these minimum and maximum solutions are listed, as well as corresponding model outputs. By definition, anhydrous solutions have F_w, B_w, and $h_w = 0$.
[c] Minimum (min) and maximum (max) source concentrations predicted by the hydrous melting equation (equation (10)).
[d] Midpoint source concentration values are used as normalizing values for all other solutions when plotting Figure 9. The input variables that created these solutions are closest to the midpoint of the range allowed for each input variable, with the exception of U_w/U_0, for which only passive upwelling ($U_w/U_0 = 1$) was allowed.

that it allows for different upwelling rates in different parts of the melting regime.

5. Results

5.1. N-MORB

[47] Figure 9a shows the compositional range of sources that can be melted to create our observed average fractionation-adjusted N-MORB concentrations of K, H_2O, Na_2O, and Ti and the observed crustal thickness of 5.7 km in the GSC "N-MORB" region (near 97°W). (See Table 5 for parameters associated with these curves.)

[48] First, we examine predictions of dry melting only. In this scenario we treat H_2O as an incompatible oxide but do not consider the effects of water on melting, i.e., equation (3), $h_w = F_w = 0$, and $U_w/U_0 = 1$. Because we consider a range of B_D values, there are a number of possible source compositions (dashed and dotted lines in Figure 9). Dry melting requires 41–53 ppm K in the source, 136–175 ppm H_2O, 2100–2600 ppm Na_2O, and 991–1136 ppm Ti. The value of $\overline{F}$ for dry melting ranges from 0.08 to 0.104, encompassing those of *Asimow and Langmuir* [2003], but extending to slightly lower values. Lower B_D values combined with a deep dry solidus (high h_D) require a less enriched source and lower $\overline{F}$ than high productivity over a shorter dry melting column (Table 5).

[49] In comparison to the dry melting solutions, consideration of a hydrous melting region reproduces our N-MORB data at lower incompatible element concentrations in the source at lower values of $\overline{F}$. Using the hydrous melting equation (equation (10)), N-MORB compositions can be produced from a source with as little as 26 ppm K, 107 ppm H_2O, 1900 ppm Na_2O, and 955 ppm Ti, and $\overline{F}$ as low as 0.046. This low $\overline{F}$ solution is predicted with h_w = 26 km, B_w = 0.04%/km, U_w/U_0 = 2, h_D = 54 km, and B_D = 0.27%/km. Passive hydrous melting ($U_w/U_0 = 1$) with h_w = 36 km and B_w = 0.03%/km plus anhydrous melting with h_D = 41.5 km and B_D = 0.49%/km requires the maximum source concentration: 35 ppm K, 141 ppm H_2O, 2400 ppm Na_2O, and 1113 ppm Ti. Concentrations between these extreme values are also viable, but created by different combinations of the above variables.

[50] These N-MORB results elucidate the importance of source H_2O and variable flow in the mantle. As emphasized by *Asimow and Langmuir*

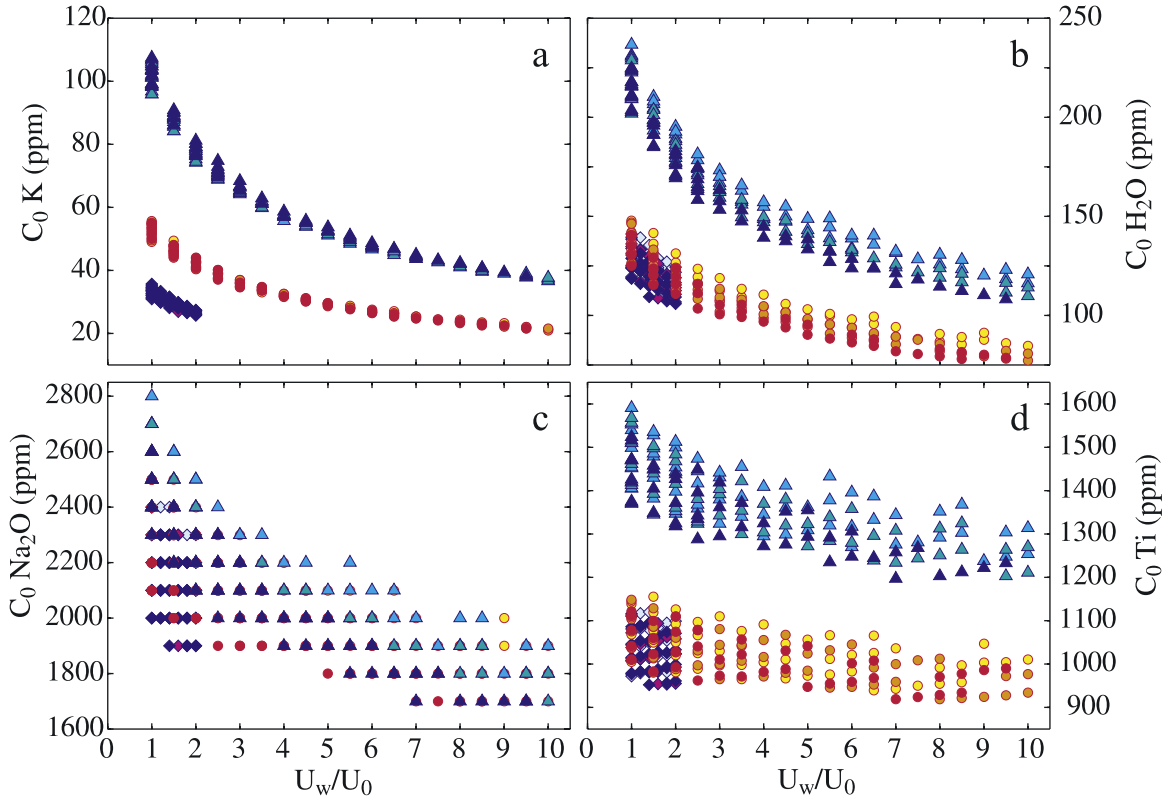

Figure 10. Mantle flow parameter U_w/U_0 versus required source compositions for N-, T-, and E-MORBs. N-MORB solutions are diamonds; T-MORB solutions are circles; and E-MORB solutions are triangles. Color variations within each MORB type represent different input values for wet productivities (B_w = 0.03%/km, 0.04%/km, and 0.05%/km); lighter colors represent lower B_w values. The more material that is cycled through the hydrous melting region relative to the anhydrous melting region (i.e., the greater U_w/U_0), the less "enriched" the source is required to be.

[2003], hydrous melting produces N-MORB solutions with lower average degrees of melting than the anhydrous pooled melting equation, thus reducing the required concentrations of the incompatible elements in the mantle source and the required temperature of the mantle.

5.2. E-MORB and T-MORB

[51] In evaluating the E-MORB and T-MORB data, we consider several important questions. Is an enriched mantle in the E-MORB region required to explain major and minor element basalt compositions that are incompatible-element enriched relative to N-MORB? Is plume-driven upwelling required? What are the effects of variable productivities within the hydrous melting region? What is the additional depth to the hydrous solidus? Must E-MORB be produced by elevated mantle temperatures relative to N-MORB?

[52] Figure 9 compares the maximum and minimum source compositions required for each MORB type for solutions to both the hydrous (equation (10)) and anhydrous equations (equation (3)). All solutions are normalized to the source values for the N-MORB "midpoint." E-MORB solutions span a large range of possible source concentrations, which encompasses nearly the entire range of N-MORB solutions. Many, but not all, of the E-MORB solutions require a more enriched source than for N-MORB. T-MORB solutions span a range that includes solutions with both higher and lower source concentrations than the maximum and minimum N-MORB solutions, respectively, although T-MORB maximum values for H_2O, Na_2O, and Ti are only very slightly greater than N-MORB maximum values. Parameters corresponding with each of the lines plotted on Figure 9 are reported in Table 5.

[53] The required source concentration depends strongly on the mantle flow parameter U_w/U_0 (Figures 9 and 10). Greater U_w/U_0 requires less source enrichment. The dependence on U_w/U_0 is strongest for the most incompatible element, K; K values of E-MORB can be produced from N-MORB source compositions only at $U_w/U_0 \geq 10$.

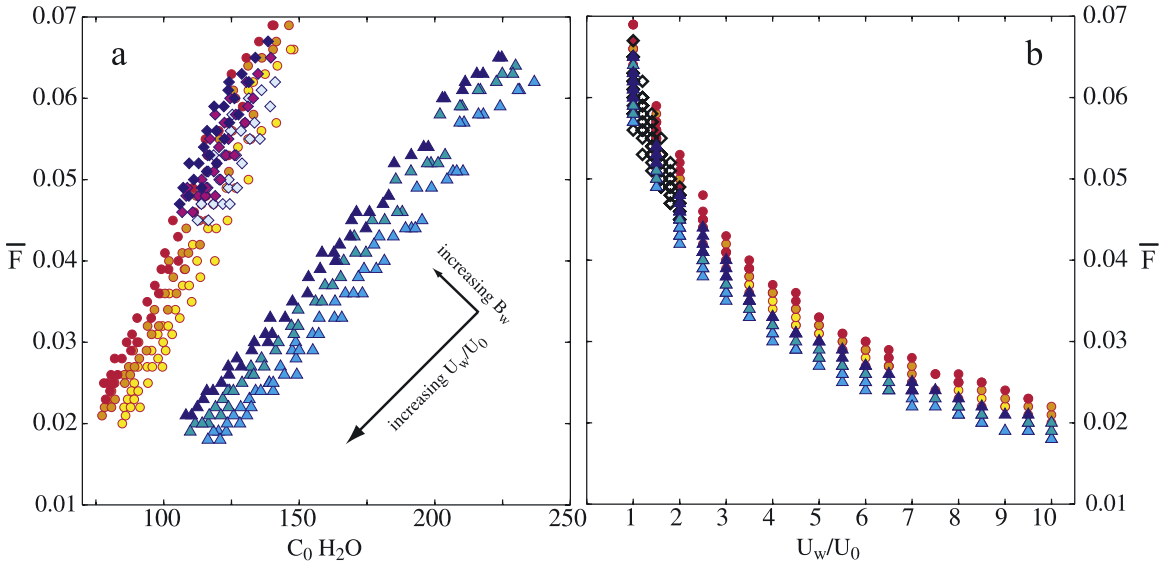

Figure 11. (a) Comparison between the allowable ranges of C_0^{H2O} and $\overline{F}$ that fit observed values of crustal thickness and average fractionation corrected compositions of the N-, T-, and E-MORB types. Symbols as in Figure 10. N-MORB solutions are confined to relatively high values of $\overline{F}$ at relatively low values of source H_2O. T-MORB solutions encompass the entire range of N-MORB $\overline{F}$ solutions but reach much lower $\overline{F}$ values than N-MORBs because T-MORB models were allowed to vary over a larger range of U_w/U_0 values. The positive correlation between C_0^{H2O} and $\overline{F}$ within each MORB type does not represent a generic trend for hydrous melting, but rather reflects the fact that all solutions for each MORB type are matches to one value of Z_{cr} and observed magma composition. The mantle flow parameter U_w/U_0 dominates the large range of both C_0^{H2O} and $\overline{F}$. (b) Illustration of $\overline{F}$ dependence on U_w/U_0; N-MORB symbols are shown with a heavy black outline for clarity.

T-MORB require a source enriched in K relative to that for N-MORB only at $U_w/U_0 \leq 3$, but not for greater values of U_w/U_0. Neither T-MORB nor E-MORB require Na-enrichment, although at low U_w/U_0 some T- and E-MORB solutions have slightly higher Na contents than the N-MORB sources. At $U_w/U_0 \geq 5$, some E- and T-MORB solutions require sources with less Na than N-MORB. For Ti, the E-MORB compositions require at least some source enrichment for all values of U_w/U_0. The Ti content of the T-MORB source does not vary significantly from that of the N-MORB source. The required source concentration also depends, although less significantly, upon B_w. In general, the more "productive" the hydrous melting region, the less source enrichment is required (Figure 10).

[54] The above results pertain only to the K, Na, Ti and H_2O variability of mantle sources contributing to average N-, T-, and E-MORB magmas along the western GSC. Geochemical data not considered in this model obviously can be used to further constrain source components along the GSC. Although our models do not require the sources for T-MORB and E-MORB to be enriched in Na relative to that for N-MORB, other data suggest that mantle sources contributing to the production of T-MORB and E-MORB along the western GSC have radiogenic isotope and highly incompatible-element ratios that are distinct from those involved in the production of N-MORB [e.g., *Schilling et al.*, 1982, 2003; *Verma and Schilling*, 1982; *Verma et al.*, 1983].

[55] The relationship between the source concentration of H_2O and $\overline{F}$ is shown in Figure 11a. The model allows E-MORB mantle to contain as little as ~110 ppm H_2O or as much as ~240 ppm, compared to between 110 and 140 ppm H_2O in our N-MORB mantle and 80–150 ppm in our T-MORB mantle. Mean degree of melting for E-MORB may be 0.019 to 0.067, depending on U_w/U_0 and productivity in the hydrous region (B_w). By comparison, mean extent of melting for the N-MORB could range from 0.046 to 0.062, and for T-MORB could range from 0.021 to 0.069. $\overline{F}$ is dominantly controlled by U_w/U_0 with increasing U_w/U_0 producing lower $\overline{F}$ (Figure 11b). For the range of U_w/U_0's (≤ 2) examined for the N-MORB data, models cannot resolve a difference in mean $\overline{F}$ between the N-MORB and E-MORB. Thus, if indeed E-MORB are created by lower $\overline{F}$ than N-MORB, as inferred from SiO_2, and CaO/Al_2O_3

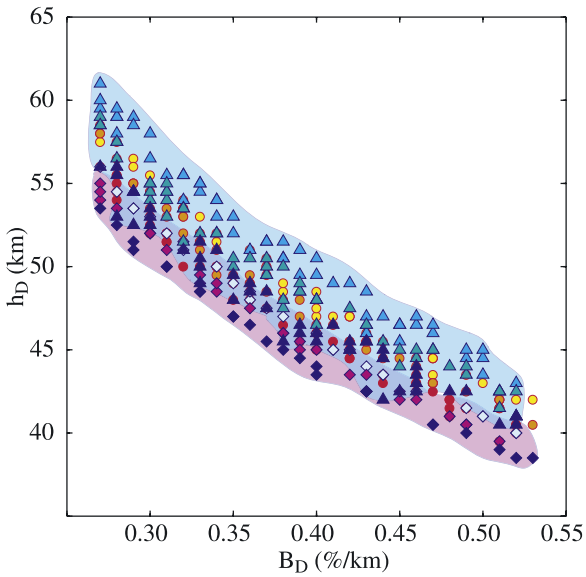

Figure 12. Depth interval of dry melting, h_D, plotted as a function of productivity in the anhydrous melting region, B_D, for each MORB type. Symbols as in Figure 10. Shaded fields encompass the range of solutions for N-MORB (pink) and E-MORB (light blue). The B_D values we allowed as viable solutions (0.27–0.53%/km, or ~0.8–1.6%/kbar) limit the maximum and minimum h_D values. At the same B_D value, the maximum difference in h_D between N-MORBs and E-MORBs is ~9 km, which can be converted to a temperature difference, ΔT, using the slope of the mantle solidus (we use 3.8°C/km). The maximum ΔT between N-MORBs and E-MORBs at constant B_D value solutions is ~34°C. When similar B_w values are compared between N- and E-MORB regions, this difference reduces to as little as 3 km, or ~11°C.

values [see also *Asimow and Langmuir*, 2003], there must be more plume-driven excess flow in the E-MORB region than in the N-MORB region.

[56] We explore the range of possible values of h_D, the depth interval of dry melting, for N-, T-, and E-MORB in Figure 12. From equation (9), the range of permissible h_D values is limited largely by our specified range of B_Ds, with larger h_Ds resulting from lower values of B_D. E-MORB solutions for h_D are between 41.5 and 54 km, T-MORB solutions range from 42 to 49.5 km, and N-MORB range from 45 to 51.5 km. Figure 12 also shows that for similar B_D values, the difference in dry solidus depth Δh_D, and therefore the temperature difference ΔT between N-MORB and E-MORB, is quite small. At any given B_D value, the maximum Δh_D between N-MORB and E-MORB solutions is 9 km. To convert Δh_D to ΔT, we fit a line to the solidus-pressure function of *Hirschmann* [2000] in the appropriate pressure range to derive the slope,

$$dT/dh_D = 3.8^\circ\mathrm{C/km}. \quad (14)$$

Our results suggest that the maximum potential temperature difference between N-MORB and E-MORB (ΔT) is ~34°C. When similar B_w values are compared between N- and E-MORB regions, this difference reduces to as little as Δh_D = 3 km, or ΔT ~ 11°C. T-MORB depths and temperatures are very similar to those for N-MORB. Thus our model indicates that the Galápagos "hot spot" increases the temperature of the mantle beneath the inflated portion of the GSC by only a few tens of degrees relative to our model N-MORB mantle, and this temperature difference is required in the E-MORB region alone; i.e., for the elements considered here, no mantle thermal anomaly is required west of 92.7°W. The thermal anomaly of 11–34°C predicted by our model is less than the ~40°C anomaly predicted by *Asimow and Langmuir* [2003], which reflects the incorporation of higher upwelling rates close to the Galapagos hot spot in our models. The range we predict is similar to the ~30°C anomaly predicted by *Canales et al.* [2002] on the basis of modeling of gravity anomalies in the region.

6. Most Likely Solutions for G′ Data

[57] In order to assess the full range of potential solutions to our G-PRIME data, we have allowed a generous range of variables. However, we may reasonably constrain our results further in an attempt to produce most-likely solutions for the different regions of the GSC. We further limit the solutions using the following arguments.

[58] 1. Crustal thickness, axial morphology, and the N-MORB composition are typical of normal mid-ocean ridge basalts globally. We therefore infer that plume-driven mantle flow is negligible in generating N-MORB, eliminating all N-MORB solutions for $U_w/U_0 > 1$. We allow E-MORB solutions only for $U_w/U_0 > 1$, as required if the inference that E-MORB are the products of lower $\overline{F}$ compared to N-MORB is true, and as argued by *Canales et al.* [2002] on the basis of gravity modeling.

[59] 2. Expecting a constant average productivity in the anhydrous region along the ridge, we narrow our B_D range to between 0.36 and 0.42%/km [*Asimow et al.*, 2001, Figure 4] for all MORB types.

[60] 3. Although some enrichment in the incompatible elements, as well as in radiogenic isotopes, in the E-MORB and T-MORB regions may be necessary to explain the data, it is unlikely that the plume-affected region(s) are depleted in these elements relative to the N-MORB region. Thus we eliminated all T- or E-MORB solutions with source concentrations of Na that are less than N-MORB solutions remaining after steps 1–3.

[61] 4. Finally, we assume that the additional zone of hydrous melting is at least as deep in the T- and E-MORB regions as in the N-MORB region. We eliminate any solutions where h_w for the T-MORB or E-MORB source was less than h_w for the N-MORB source.

[62] These additional constraints considerably narrow the range of solutions. They imply that GSC N-MORB were created by melting of a passively upwelling source with ~35 ppm K, ~130 ppm H_2O, 2300 ppm Na_2O, and 1050 ppm Ti. Mean degree of melting is ~0.06, and the maximum degree of melting is ~0.20. Hydrous melting spanned a depth interval (h_w) of ~30 km, and dry melting spanned a depth interval (h_D) of ~50 km. Model output uncertainties are typically <10% of the above solutions, but the uncertainties associated with the simplifying assumptions inherent to the methodology are likely to be larger.

[63] If T-MORB were created by any plume-driven mantle flow, it is less than $U_w/U_0 = 2$. Solutions produced at higher U_w/U_0 values are ruled out by restrictions (3) and (4). Of the elements considered in our model, T-MORB parental magma compositions vary from those for N-MORB only in the highly incompatible element, K. This variation can be explained by either slightly higher $\overline{F}$ of a source with only a few ppm more H_2O than the N-MORB source (when $U_w/U_0 = 1$), or slightly lower $\overline{F}$ of a source with a few ppm less H_2O than for N-MORB (when $U_w/U_0 = 1.5$ for T-MORB) (Figure 13). These results indicate that T-MORB can be created by melting a source very similar to the N-MORB source with only K enriched by ~50%. Within the range of model uncertainty, values of source Na, Ti and H_2O, $\overline{F}$, F_{max}, h_w, and h_D are indistinguishable from those in the N-MORB region.

[64] The maximum excess mantle flow in the E-MORB region allowed by restrictions (3) and (4) is $U_w/U_0 = 3.5$. This limits the minimum $\overline{F}$ of E-MORB to 0.03, and requires that E-MORB

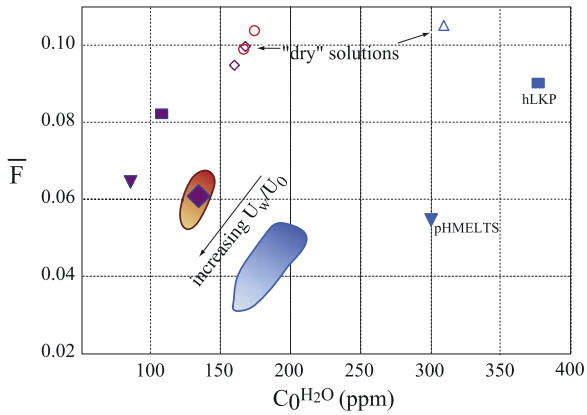

Figure 13. Modeling solutions for Galápagos spreading center compositions. Solutions to G′ data using the hydrous melting equation (equation (10)) and restricting the range of input parameters to those that are most likely (see text for discussion of parameters) are shown as large filled symbols and fields. Solutions created using the anhydrous, pooled melting equation (equation (3)) (open symbols) are shown for comparison. Shading of the fields for hydrous melting solutions represents variation in the mantle flow parameter U_w/U_0. T-MORB hydrous solutions (shaded red region) encompass the limited range of N-MORB solutions (filled diamond), with lower values of T-MORB $\overline{F}$ and C_0^{H2O} resulting from $U_w/U_0 = 1.5$; higher $\overline{F}$ and C_0^{H2O} solutions are created by passive upwelling ($U_w/U_0 = 1$). Hydrous model results of *Asimow and Langmuir* [2003, Table 2] are shown for comparison; this study applied new hydrous melting models (hLKP, squares; pHMELTS, inverted triangles) (see *Asimow and Langmuir* [2003] for details) to published geochemical data from 85–87°W (N-MORB, purple symbols) and 90–92°W (E-MORB, blue symbols). Both models of *Asimow and Langmuir* [2003] as well as our results indicate reduction in required $\overline{F}$ for hydrous solutions compared to anhydrous solutions. Our model is consistent with pHMELTS in having E-MORB form at lower $\overline{F}$ than for N-MORB. Our modeling suggests that the sources that melted to produce E-MORB are significantly less enriched in water than the models of *Asimow and Langmuir* [2003]. See text for discussion.

have at least some K and H_2O source enrichment relative to N-MORB and T-MORB. Our results indicate that relative to the N-MORB source, E-MORB represent the products of melting a source enriched in K by ~150% (75 ppm), H_2O by 50% (190 ppm), Na_2O by <10% (2400 ppm), and Ti by ~40% (1450 ppm). Compared to the N-MORB region, the depth interval of hydrous melting is ~40% greater in the E-MORB region. Differences in anhydrous melting between the two regions are not different within resolution, but given the model uncertainties for h_D, this result allows for only a

slight temperature anomaly beneath the E-MORB region of <20°C.

7. Global and Local Implications

[65] Even the most "normal" mid-ocean ridges contain some amount of water [*Michael and Chase*, 1987; *Dixon et al.*, 1988; *Michael*, 1995; *Danyushevsky et al.*, 2000]. Our equations that take into account the "extra" region (no matter how small or large) of low-degree partial melts contributed by the presence of water have implications for the concept of "typical" degrees of melting at mid-ocean ridges, and for the composition of incompatible-element-depleted mantle from which MORB are generated. Normal mid-ocean ridges are commonly considered to be produced by mean extents of melting of ~10% from a melting column on the order of 60 km deep, producing ~6 km of crust [e.g., *Klein et al.*, 1991; *Langmuir et al.*, 1992; *Forsyth*, 1993].

[66] Recent works by several authors, including the present study, indicate that these values should be reevaluated. We estimate that GSC N-MORB were created by $\overline{F} \sim 6\%$. *Forsyth* [1993] and *Plank et al.* [1995], who defined "mean F" as the mean value of $F(F_v)$ for melts pooled from the melting region (as opposed to F_B, bulk melt fraction), concluded that average N-MORB are produced by ~6.67% melting. *Asimow et al.* [2001] predicted a mean melt fraction of no more than 8% for N-MORB, whereas *Asimow and Langmuir* [2003], using new (pHMELTS) algorithms, predicted F_B as low as 6.5% for normal regions of the Galápagos Spreading Center. There are two important and related results of the explicit consideration of the effects of water on the melting of MORB mantle. Incorporation of a region of hydrous melting reduces significantly the mean extent of melting required to produce normal MORB. A consequence of the reduction in mean extent of melting is that the composition of the mantle beneath even "normal" segments of mid-ocean ridges can be even more depleted in incompatible elements than was previously allowed by dry melting equations [*Asimow and Langmuir*, 2003; *Asimow et al.*, 2004; this study].

[67] The explicit incorporation of plume-driven, enhanced mantle flow through the melting zone has important consequences for a number of melting parameters close to the Galápagos hot spot. For example, we require only about 50% enrichment in mantle H_2O in the E-MORB region, compared to ~250% increases in the models of *Asimow and Langmuir* [2003] (Figure 13). The thermal anomaly suggested by our model (<20°C) is about half that predicted by *Asimow and Langmuir* [2003]. In general, incorporation of enhanced flow greatly reduces the magnitude of the thermal and compositional anomaly required to explain the Galápagos bathymetric and chemical anomaly. If enhanced upwelling is a direct consequence of compositional or thermal variations in the mantle, then models that neglect this important process will tend to over-estimate the magnitude of the anomaly in the mantle.

[68] A geodynamic model of mantle flow and melting that is consistent with a small temperature anomaly and plume-driven, excess mantle flow was presented by *Ito et al.* [1997]. This model simulated a mantle plume stem with a broad radius (200 km) and small excess temperature ($\leq$50°C) beneath the Galápagos archipelago. The model predicted this "warm" plume material to flow north to the GSC melting zone and generate along-axis crustal thickness variations, consistent with the results of G′. Recent seismic studies including tomographic inversions of P and S body waves [*Toomey et al.*, 2001] and receiver functions analyses [*Hooft et al.*, 2003] suggest the presence of a mantle plume beneath the Galápagos archipelago, but a plume stem of higher excess temperature and smaller radius than that simulated by *Ito et al.* [1997]. To reconcile these results with ours, it is possible that the seismic tomography is imaging a narrow region of excess melting and melt retention rather than a region of narrow and high excess temperature. The receiver function study, which imaged a thinning of the mantle transition zone beneath the archipelago, however, would not be sensitive to melt in the upper mantle. Thus another possibility is that a narrow, high temperature anomaly at the center of the Galápagos plume is sheathed by a broader region of low excess temperature. If so, this "warm" material will likely have the most influence on the volume and composition of melts erupting along the GSC, which is consistent with our results. Further analyses of existing seismic data, as well as more complete seismic data coverage of the area is needed to test these possibilities. Also, the constraints on the nature of the mantle source and conditions of melting that we have placed in this study equip future geochemical studies to better address issues regarding the mechanisms of mass transport and

chemical mixing of Galápagos plume material along the GSC.

8. Conclusions

[69] 1. Samples collected from the GSC can be classified as E-, T-, or N-MORB on the basis of K/Ti ratios >0.15, 0.15 to 0.09, and <0.09, respectively. High K/Ti E-MORB also have higher H_2O, Al_2O_3, and Na_2O, and lower FeO*, SiO_2, and CaO/Al_2O_3 relative to N-MORB at similar values of MgO. T- and E-MORB may be further subdivided into T1, T2, T3, E1, and E2 on the basis of CaO/Al_2O_3 ratios, SiO_2 content, and subtle variations in incompatible elements.

[70] 2. E-MORB dominate the GSC east of 92.6°W, where the crust is thickest (6.5–8 km). T-MORB are mainly found between 92.6°W and 95.5°W, where crustal thickness is 6–7 km. West of the propagating rift tip at 95.5°W, where crustal thickness is <6 km, N-MORB dominate. E-MORB incompatible element concentrations, including fractionation-corrected values for H_2O, peak near 91.8°W and decrease with increasing distance from the hot spot. $Fe_{8.0}$, $Si_{8.0}$, and $Ca_{8.0}/Al_{8.0}$ all show their lowest values near 91.8°W.

[71] 3. Geochemical boundaries correlate with geophysical and morphological characteristics. The transition from N-MORB to T-MORB occurs at the 95.5°W propagating rift tip, which also marks the boundary between axial rift-valley morphology and transitional morphology. Near 92.7°W, morphology changes from transitional to an axial high, the axial magma chamber seismic reflector shoals by >1 km, the thickness of seismic layer 2A diminishes by half, and lavas become dominated by E-MORB.

[72] 4. Our new melting model considers the effects of an ''additional'' zone of hydrous melting that is created by the depression of the mantle solidus in the presence of water in the mantle. Variables in the equation include depth interval of the additional hydrous melting (h_w), the fraction of melt liberated per unit of depth of decompression in the hydrous region (productivity, B_w), source concentration (C_0) of incompatible elements, including H_2O, and the flow rate of mantle passing through the hydrous region relative to the anhydrous region (U_w/U_0). Incompatible element concentrations in pooled magmas are predicted to increase with height h_w and U_w/U_0. Of these variables, U_w/U_0 has the strongest effect on $\overline{F}$, with higher U_w/U_0 values corresponding to lower $\overline{F}$.

[73] 5. We use this hydrous melting equation to model the variables that may combine to match the crustal thickness and average values of fractionation-corrected K_2O, Na_2O, H_2O, and TiO_2 in lavas measured along the GSC. We estimate that GSC N-MORB were created by $\overline{F}$ ~0.06 from a source with ~35 ppm K, 130 ppm H_2O, 2300 ppm Na_2O, and 1050 ppm Ti. The absolute value of $\overline{F}$ depends on the effect of a small amount of water on the position of the solidus, but is estimated to be $\overline{F}$ ~0.06. We estimate $h_w \sim 30–40$ km and $h_D \sim 40–50$ km.

[74] 6. The extreme bounds that we consider in our model parameters suggest that the E-MORB region must be enriched in K unless the upwelling rate is >10. E-MORB $\overline{F}$ may be as low as 0.02 if $U_w/U_0 = 10$, or as high as 0.065 if $U_w/U_0 = 1$. The E-MORB source may have as little as 110 ppm H_2O or as much as 240 ppm H_2O with a hydrous melting depth interval in the range of $h_w = 30–60$ km (assuming h_w/C_0^{H2O} of 0.25 km/ppm) and a depth interval of dry melting of $h_D = 45–60$ km. We estimate a maximum temperature anomaly ΔT of ~34°C in the E-MORB region compared to the N-MORB region. With the above conditions of hydrous melting we can explain the geochemical evidence for lower $\overline{F}$ as well as geophysical observations suggesting greater magma production nearest the Galapagos hot spot. The direct effect of water on the major element composition of these magmas may be an additional factor contributing to decreasing SiO_2, FeO, MgO, and CaO near the hot spot [*Gaetani and Grove*, 1998].

[75] 7. Our preferred conditions required to explain the total variation in crustal thickness and glass compositions along the western GSC are only a slight temperature increase (<20°C), coupled with a moderately enriched mantle source and plume-driven, deep mantle flow of $U_w/U_0 = 1.5–3.5$.

[76] 8. Incorporation of enhanced deep mantle flow close to the hot spot further reduces the required magnitude of the thermal and compositional anomaly required to explain the gradients in chemical composition and crustal thickness along the GSC.

Acknowledgments

[77] We are grateful to the captain, crew, and shipboard scientific party of R/V *Maurice Ewing* Cruise EW0004 for their help with data acquisition at sea. The Ecuadorian government and the Parque Nacional Galápagos permitted work in their territorial waters. JoAnn Sinton put excessive care and extreme hours into sample preparation. Discussions with Mark Behn, Pablo Canales, Bob Detrick, Dave Graham,

Charlie Langmuir, John Mahoney, and Brian Taylor were helpful in various aspects of this study. We are grateful to Charlie Langmuir and Peter Michael for thorough and detailed reviews and to Dave Graham and Bill White for additional comments and suggestions, which led to substantial improvement. Many figures in this paper were prepared using the GMT software package [*Wessel and Smith*, 1998]. This work was supported by NSF grants OCE98-18632 to the University of Hawai'i, OCE-0002189 to the UC Davis, and OCE99-0000478 to the University of Miami. This is SOEST contribution 6396.

References

Anderson, R., D. Clague, K. Klitgord, M. Marshall, and R. Nishimori (1975), Magnetic and petrologic variations along the Galápagos Spreading Center and their relation to the Galápagos melting anomaly, *Bull. Geol. Soc. Am.*, *86*, 683–694.

Asimow, P. D., and C. H. Langmuir (2003), The importance of water to oceanic melting regimes, *Nature*, *421*, 815–820.

Asimow, P. D., M. M. Hirschmann, and E. M. Stolper (2001), Calculation of peridotite partial melting from thermodynamic models of minerals and melts, IV. Adiabatic decompression and the composition and mean properties of mid-ocean ridge basalts, *J. Petrol.*, *42*(5), 963–998.

Asimow, P. D., J. E. Dixon, and C. H. Langmuir (2004), A hydrous melting and fractionation model for mid-ocean ridge basalts: Application to the Mid-Atlantic Ridge near the Azores, *Geochem. Geophys. Geosyst.*, *5*, Q01E16, doi:10.1029/2003GC000568.

Bell, D. R., G. R. Rossman, J. Maldener, D. Endisch, and F. Rauch (2003), Hydroxide in olivine: A quantitative determination of the absolute amount and calibration of the IR spectrum, *J. Geophys. Res.*, *108*(B2), 2105, doi:10.1029/2001JB000679.

Bonatti, E. (1990), Not so hot "hot spots" in the oceanic mantle, *Science*, *250*, 107–111.

Braun, M. G., G. Hirth, and E. M. Parmentier (2000), The effects of deep damp melting on mantle flow and melt generation beneath mid-ocean ridges, *Earth Planet. Sci. Lett.*, *176*, 339–356.

Canales, J. P., J. J. Danobeitia, R. S. Detrick, E. E. E. Hooft, R. Bartolomé, and D. Naar (1997), Variations in axial morphology along the Galápagos Spreading Center and the influence of the Galápagos hotspot, *J. Geophys. Res.*, *102*, 27,341–27,354.

Canales, J. P., G. Ito, R. S. Detrick, and J. Sinton (2002), Crustal thickness along the western Galápagos Spreading Center and the compensation of the Galápagos hotspot, *Earth Planet. Sci. Lett.*, *203*, 311–327.

Christie, D. M., and J. M. Sinton (1981), Evolution of abyssal lavas along propagating segments of the Galápagos Spreading Center, *Earth Planet. Sci. Lett.*, *56*, 321–335.

Christie, D. M., and J. M. Sinton (1986), Major element constraints on melting, differentiation and mixing of magmas from the Galápagos 95.5°W propagating rift system, *Contrib. Mineral. Petrol.*, *94*, 274–288.

Danyushevsky, L., S. Eggins, T. Falloon, and D. Christie (2000), H_2O abundance in depleted to moderately enriched mid-ocean ridge magmas; part I: Incompatible behaviour, implications for mantle storage, and origin of regional variations, *J. Petrol.*, *41*(8), 1329–1364.

DeMets, C., R. G. Gordon, D. F. Argus, and S. Stein (1994), Effect of recent revisions to the geomagnetic reversal time scale on estimates of current plate motions, *Geophys. Res. Lett.*, *21*, 2191–2194.

Detrick, R. S., J. M. Sinton, G. Ito, J. P. Canales, M. Behn, T. Blacic, B. Cushman, J. E. Dixon, D. W. Graham, and J. J. Mahoney (2002), Correlated geophysical, geochemical, and volcanological manifestations of plume-ridge interaction along the Galápagos Spreading Center, *Geochem. Geophys. Geosyst.*, *3*(10), 8501, doi:10.1029/2002GC000350.

Dixon, J. E., and D. A. Clague (2001), Volatiles in basaltic glasses from Loihi Seamount, Hawaii: Evidence for a relatively dry plume component, *J. Petrol.*, *42*, 627–654.

Dixon, J. E., E. M. Stolper, and J. R. Delaney (1988), Infrared spectroscopic measurements of CO_2 and H_2O glasses in the Juan de Fuca Ridge basaltic glasses, *Earth Planet. Sci. Lett.*, *90*, 87–104.

Fisk, M. R., A. E. Bence, and J.-G. Schilling (1982), Major element chemistry of Galápagos rift zone magmas and their phenocrysts, *Earth Planet. Sci. Lett.*, *61*, 171–189.

Forsyth, D. (1993), Crustal thickness and the average depth and degree of melting in fractional melting models of passive flow beneath mid-ocean ridges, *J. Geophys. Res.*, *98*, 16,073–16,079.

Gaetani, G., and T. Grove (1998), The influence of water on melting of mantle peridotite, *Contrib. Mineral. Petrol.*, *131*, 323–346.

Geist, D. J. (1992), An appraisal of melting processes and the Galápagos hotspot: Major- and trace-element evidence, *J. Volcanol. Geotherm. Res.*, *52*, 65–82.

Hekinian, R., G. Thompson, and D. Bideau (1989), Axial and off-axial heterogeneity of basaltic rocks from the East Pacific Rise at 12°35′N–12°51′N and 11°26′N–11°30′N, *J. Geophys. Res.*, *94*, 17,437–17,463.

Hey, R. N., et al. (1992), ALVIN Investigation of an active propagating rift system, Galápagos 95.5°W, *Mar. Geophys. Res.*, *14*, 207–226.

Hirschmann, M. M. (2000), Mantle solidus: Experimental constraints and the effects of peridotite composition, *Geochem. Geophys. Geosyst.*, *1*, Paper number 2000GC000070.

Hirschmann, M. M., P. D. Asimow, M. S. Ghiorso, and E. M. Stolper (1999), Calculation of peridotite partial melting from thermodynamic models of minerals and melts. III. Controls on isobaric melt production and the effect of water on melt production, *J. Petrol.*, *40*(5), 831–851.

Hirth, G., and D. Kohlstedt (1996), Water in the oceanic upper mantle: Implications for rheology, melt extraction and the evolution of the lithosphere, *Earth Planet. Sci. Lett.*, *144*, 93–108.

Hooft, E. E. E., D. R. Toomey, and S. C. Solomon (2003), Anomalously thin transition zone beneath the Galapagos hotspot, *Earth Planet. Sci. Lett.*, *216*, 55–64.

Ito, G., and J. J. Mahoney (2002), Effects of variable productivity and active mantle of upwelling on trace-elements and isotopic composition of hotspot magmas, *Eos Trans. AGU*, *83*(47), Fall Meet. Suppl., Abstract S71D-06.

Ito, G., J. Lin, and C. Gable (1997), Interaction of mantle plumes and migrating mid-ocean ridges: Implications for the Galápagos plume-ridge system, *J. Geophys. Res.*, *102*, 15,403–15,417.

Ito, G., Y. Shen, G. Hirth, and C. Wolfe (1999), Mantle flow, melting, and dehydration of the Iceland mantle plume, *Earth Planet. Sci. Lett.*, *165*, 81–96.

Johnson, K., H. Dick, and N. Shimizu (1990), Melting in the oceanic upper mantle: An ion microprobe study of diopsides in abyssal peridotites, *J. Geophys. Res.*, *95*, 2661–2678.

Katz, R. F., M. Spiegelman, and C. H. Langmuir (2003), A new parameterization of hydrous mantle melting, *Geochem. Geophys. Geosyst.*, *4*(9), 1073, doi:10.1029/2002GC000433.

Klein, E., and C. Langmuir (1987), Global correlations of ocean ridge basalt chemistry with axial depth and crustal thickness, *J. Geophys. Res.*, *92*, 8089–8115.

Klein, E. M., T. Plank, and C. H. Langmuir (1991), Constraints on models for mantle melting beneath ocean ridges, *RIDGE Events*, *2*, 11–12.

Kushiro, L. (1968), The system forsterite-diopside-silica with and without water at high pressure, *Am. J. Sci.*, *267A*, 269–294.

Langmuir, C., E. Klein, and T. Plank (1992), Petrological systematics of mid-ocean ridge basalts: Constraints on melt generation beneath ocean ridges, in *Mantle Flow and Melt Generation at Mid-ocean Ridges*, *Geophys. Monogr. Ser.*, vol. 71, edited by J. P. Morgan, D. K. Blackman, and J. M. Sinton, pp. 184–280, AGU, Washington, D. C.

Maclennan, J., D. McKenzie, and K. Gronvold (2001), Plume-driven upwelling under central Iceland, *Earth Planet. Sci. Lett.*, *194*, 67–82.

McKenzie, D. P., and M. J. Bickle (1988), The volume and composition of melt generated by extension of the lithosphere, *J. Petrol.*, *29*, 625–679.

McKenzie, D., and R. K. O'Nions (1991), Partial melt distributions from inversion of rare earth element concentrations, *J. Petrol.*, *32*, 1021–1091.

Michael, P. (1988), The concentration, behavior and storage of H_2O in the suboceanic upper mantle: Implications for mantle metasomatism, *Geochem. Cosmochim. Acta*, *52*, 555–566.

Michael, P. (1995), Regionally distinctive sources of depleted MORB: Evidence from trace elements and H_2O, *Earth Planet. Sci. Lett.*, *131*, 301–320.

Michael, P., and R. L. Chase (1987), The influence of primary magma composition H_2O and pressure on mid-ocean ridge basalt differentiation, *Contrib. Mineral. Petrol.*, *96*, 245–263.

Niu, Y., D. G. Waggoner, J. M. Sinton, and J. J. Mahoney (1996), Mantle source heterogeneity and melting processes beneath seafloor spreading centers: The East Pacific Rise, 18°–19°S, *J. Geophys. Res.*, *101*(B12), 27,711–27,733.

Plank, T., and C. Langmuir (1992), Effects of the melting regime on the composition of the oceanic crust, *J. Geophys. Res.*, *97*, 19,749–19,770.

Plank, T., M. Spiegelman, C. H. Langmuir, and D. W. Forsyth (1995), The meaning of "mean F": Clarifying the mean extent of melting at ocean ridges, *J. Geophys. Res.*, *100*, 15,045–15,052.

Ribe, N., U. R. Christensen, and J. Theissing (1995), The dynamics of plume-ridge interaction, 1: Ridge-centered plumes, *Earth Planet. Sci. Lett.*, *134*, 155–168.

Schilling, J.-G., M. B. Bergeron, and R. Evans (1980), Halogens in the mantle beneath the north Atlantic, *Philos. Trans. R. Soc. London*, *297*, 147–178.

Schilling, J.-G., R. H. Kingsley, and J. D. Devine (1982), Galápagos hot spot-spreading center system I. Spatial petrological and geochemical variations (83°W–101°W), *J. Geophys. Res.*, *87*, 5593–5610.

Schilling, J. G., M. Zajac, R. Evans, T. Johnston, W. White, J. D. Devine, and R. Kingsley (1983), Petrologic and geochemical variations along the Mid-Atlantic Ridge from 29°N to 73°N, *Am. J. Sci.*, *283*, 510–586.

Schilling, J.-G., D. Fontignie, J. Blichert-Toft, R. Kingsley, and U. Tomza (2003), Pb-Hf-Nd-Sr isotope variations along the Galápagos Spreading Center (101°–83°W): Constraints on the dispersal of the Galápagos mantle plume, *Geochem. Geophys. Geosyst.*, *4*(10), 8512, doi:10.1029/2002GC000495.

Scott, D. R., and D. J. Stevenson (1989), A self-consistent model for melting, magma migration and buoyancy-driven circulation beneath mid-ocean ridges, *J. Geophys. Res.*, *94*, 2973–2988.

Shaw, D. M. (1970), Trace element fractionation during anatexis, *Geochem. Cosmochim. Acta*, *34*, 237–243.

Sinton, J. M., D. S. Wilson, D. M. Christie, R. N. Hey, and J. R. Delaney (1983), Petrologic consequences of rift propagation on oceanic spreading ridges, *Earth Planet. Sci. Lett.*, *62*, 193–207.

Sinton, J. M., S. M. Smaglik, J. J. Mahoney, and K. C. MacDonald (1991), Magmatic processes at superfast spreading midocean ridges: Glass compositional variations along the East Pacific Rise 13°–23°S, *J. Geophys. Res.*, *96*, 6133–6155.

Sinton, J., R. Detrick, J. P. Canales, G. Ito, and M. Behn (2003), Morphology and segmentation of the western Galápagos Spreading Center, 90.5°–98°W: Plume-ridge interaction at an intermediate spreading ridge, *Geochem. Geophys. Geosyst.*, *4*(12), 8515, doi:10.1029/2003GC000609.

Smith, W. H. F., and D. T. Sandwell (1997), Global seafloor topography from satellite altimetry and ship depth soundings, *Science*, *277*, 1957–1962.

Toomey, D. R., E. E. E. Hooft, S. C. Solomon, D. E. James, and M. L. Hall (2001), Upper mantle structure beneath the Galapagos Archipelago from body wave data, *Eos Trans. AGU*, *82*(47), Fall Meet. Suppl., Abstract F1205.

Turcotte, D. L., and J. P. Morgan (1992), The physics of magma migration and mantle flow beneath a mid-ocean ridge, in *Mantle Flow and Melt Generation Beneath Mid-ocean Ridges*, vol. 71, edited by J. P. Morgan, D. K. Blackman, and J. M. Sinton, pp. 155–182, AGU, Washington, D. C.

Verma, S. P., and J.-G. Schilling (1982), Galápagos hot spot-spreading center system: 2. $^{87}Sr/^{86}Sr$ and large ion lithophile element variations (85°W–101°W), *J. Geophys. Res.*, *87*, 10,838–10,856.

Verma, S. P., J.-G. Schilling, and D. G. Waggoner (1983), Neodymium isotopic evidence for Galápagos hotspot-spreading center system evolution, *Nature*, *306*, 654–657.

Wessel, P., and W. H. F. Smith (1998), New, improved version of the Generic Mapping Tools released, *Eos Trans. AGU*, *79*, 579.

White, W. M., A. R. McBirney, and R. A. Duncan (1993), Petrology and geochemistry of the Galápagos Islands: Portrait of a pathological mantle plume, *J. Geophys. Res.*, *98*, 19,533–19,563.

Yonover, R. N. (1989), Petrological effects of rift failure at the Galápagos Spreading Center near 95.5°W including analyses of glass inclusions by laser mass spectrometry and ion microprobe, Ph.D. dissertation, 193 pp., Univ. of Hawaii, Honolulu.